Open access • Journal Article • DOI:10.1017/S0022112008005090

Three-dimensional instantaneous structure of a shock wave/turbulent boundary layer interaction — Source link

R.A. Humble, Gerrit E. Elsinga, Fulvio Scarano, B. W. van Oudheusden

Institutions: Delft University of Technology

Published on: 31 Dec 2009 - Journal of Fluid Mechanics (Cambridge University Press)

Topics: Boundary layer, Shock wave, Mach number, Particle image velocimetry and Supersonic speed

J. Fluid Mech. (2009), *vol.* 622, *pp.* 33–62.
doi:10.1017/S0022112008005090 Printed in the United Kingdom

Three-dimensional instantaneous structure of a shock wave/turbulent boundary layer interaction

R. A. HUMBLE†, G. E. ELSINGA, F. SCARANO AND B. W. VAN OUDHEUSDEN

Faculty of Aerospace Engineering, Delft University of Technology, Kluyverweg 1, 2629 HS, Delft, The Netherlands

(Received 1 November 2007 and in revised form 3 September 2008)

An experimental study is carried out to investigate the three-dimensional instantaneous structure of an incident shock wave/turbulent boundary layer interaction at Mach 2.1 using tomographic particle image velocimetry. Large-scale coherent motions within the incoming boundary layer are observed, in the form of three-dimensional streamwise-elongated regions of relatively low- and high-speed fluid, similar to what has been reported in other supersonic boundary layers. Three-dimensional vortical structures are found to be associated with the low-speed regions, in a way that can be explained by the hairpin packet model. The instantaneous reflected shock wave pattern is observed to conform to the low- and high-speed regions as they enter the interaction, and its organization may be qualitatively decomposed into streamwise translation and spanwise rippling patterns, in agreement with what has been observed in direct numerical simulations. The results are used to construct a conceptual model of the three-dimensional unsteady flow organization of the interaction.

1. Introduction

One of the most engaging yet perplexing phenomena in high-speed fluid dynamics is the interaction between a shock wave and a turbulent boundary layer (SWTBLI). Such interactions occur in a wide variety of internal and external aeronautical applications, and a detailed understanding of the flow physics remains a necessary prerequisite for accurate flow-field prediction, efficient design of high-speed aerospace vehicles, as well as advances in combustion processes (Dolling 2001). A vast body of research has therefore been accumulated over the years describing the interaction's most salient features. Reviews of much of the early work, concerning two-dimensional interactions, may be found in Green (1970), Hankey & Holden (1975), and Adamson & Messiter (1980). More recent reviews, with emphasis on the unsteadiness properties, including three-dimensional interactions, may be found in Délery & Marvin (1986), Dolling (2001), and Smits & Dussauge (2006).

One aspect that has attracted particular attention has been the large-scale unsteadiness of the shock wave system and pulsating of the interaction zone, particularly in view of the relatively large discrepancy between the dominant frequencies of the shock motion and the characteristic frequency of the incoming boundary layer. As noted by Wu & Martin (2008) for instance, numerous studies

† Email address for correspondence: r.a.humble@tudelft.nl

have reported that the time scale of the large-scale low-frequency motion is of the order $10\delta/U_\infty$–$100\delta/U_\infty$ (see e.g. Dolling 2001; Dussauge, Dupont & Debiève 2006), in contrast to the characteristic time scale of the incoming boundary layer δ/U_∞, where δ is the boundary layer thickness and U_∞ is the free-stream velocity. A better understanding of this large-scale unsteadiness is important to mitigate the premature structural fatigue caused by the intense fluctuating wall pressures and heat transfer that accompany shock oscillation (Dolling 2001), as well as the recognized deficiencies of some of the most promising turbulence closure models, which seem to indicate the necessity of incorporating large-scale unsteady effects in order to properly predict mean flow quantities (Knight & Degrez 1998).

Many researchers have therefore attempted to correlate this large-scale unsteadiness with a variety of physical mechanisms, yet explanations have diverged to include a number of debated and sometimes contradictory conclusions. Plotkin (1975) developed a mathematical model based on the perturbation of a shock by random fluctuations within the incoming boundary layer that was able to represent the manner in which relatively broad-band perturbations lead to relatively low-frequency motion of the separation bubble and shock system. This model was later substantiated by the experimental work of Poggie & Smits (2001), who used it in their investigation of the origins of shock unsteadiness in a reattaching shear layer. Andreopoulos & Muck (1987) suggested that the frequency of the shock wave system unsteadiness scaled on the bursting frequency of the incoming boundary layer, concluding that the turbulence of the incoming boundary layer was largely responsible for the shock wave motion. In comparison, Thomas, Putman & Chu (1994) found no discernible statistical relationship between burst events in the upstream boundary layer and shock wave motion.

Dolling & Murphy (1983) and Erengil & Dolling (1991) began a fruitful line of research, by proposing that the internal dynamics of the separated flow region are responsible for some of the low-frequency oscillations, suggesting that the large-scale motion is the result of an expansion and contraction of the separation bubble. This paved the way for more detailed studies into the cause(s) of such bubble motion. For example, Ünalmis & Dolling (1998) and Beresh, Clemens & Dolling (2002) have since found that at least some of the bubble unsteadiness is driven by low-frequency turbulent fluctuations within the upstream boundary layer, proposing that the instantaneous fullness of the incoming boundary layer velocity profile is correlated with the shock wave position via the motion of the separation bubble.

The preponderance of large-scale coherent motions within the turbulent boundary layer has also motivated workers to investigate the role of these motions within the context of SWTBLI large-scale unsteadiness. Using particle image velocimetry (PIV) in the streamwise–spanwise plane of their compression ramp interaction, Ganapathisubramani, Clemens & Dolling (2007) have observed very long regions of alternating low- and high-speed fluid within the logarithmic region of the incoming boundary layer, and proposed that they are associated with the low-frequency motion of the separated flow region and shock wave. Such features have also been observed experimentally in other supersonic boundary layers by Samimy, Arnette & Elliot (1994), Ganapathisubramani, Clemens & Dolling (2006) and Elsinga *et al.* (2007*a*), as well as computationally using direct numerical simulation (DNS) by Ringuette, Wu & Martin (2008).

Yet most of the work cited above has been carried out on compression ramp interactions, and generalizations of these models to the incident SWTBLI problem is still an open question (Dupont, Haddad & Debiève 2006). Although less

well-documented compared to its compression ramp counterpart, similar behaviour has been found in the shock reflection case, such as the low-frequency motion of the reflected shock wave when substantial boundary layer separation is involved. In particular, Pirozzoli & Grasso (2006) carried out a DNS on an incident SWTBLI at Mach 2.25 and proposed that the large-scale unsteadiness was associated with an acoustic feedback mechanism, similar to what is involved in the generation of tones in cavities and screeching jets. Also, Dupont *et al.* (2006) have experimentally obtained characteristic time and length scales of the reflected shock wave and inside the interaction, and found strong statistical evidence of a link between low-frequency shock wave movements and the downstream part of the interaction. Dussauge *et al.* (2006) have recently reviewed and analysed evidence of the large-scale unsteadiness observed in incident SWTBLIs, and concluded from the experimental results that the three-dimensional structure of the separated bubble may be at the origin of such unsteadiness. Yet to date, no comprehensive framework has been formulated in which all the results from these configurations can be satisfactorily explained, and the failure of the SWTBLI community to gain a general consensus has only reinforced the status of the interaction as an enigma.

Yet most of the quantitative experimental studies of SWTBLIs have been limited to examining flow details using single-point measurement techniques, such as hot-wire anemometry (HWA) and laser Doppler velocimetry (LDV), or planar techniques, such as PIV in particular (Dolling 2001). The inability to make instantaneous volumetric measurements often leads to ambiguities in the interpretation of the data, which necessitates various assumptions being made in order to link these reduced-dimensional representations to the three-dimensional instantaneous structure of the interaction. While numerical simulation, DNS in particular, has been instrumental in elucidating the three-dimensional dynamical features of SWTBLIs (see e.g. Pirozzoli & Grasso 2006; Wu & Martin 2007, 2008), the attendant Reynolds number limitation leaves the phenomenology at high Reynolds numbers very much an open question.

Experimentalists have therefore long been motivated, in the quantitative visualization of turbulent fluid flows, to move towards volumetric methods. Current techniques based on the PIV method include the scanning light sheet method (Brucker 1996), holographic PIV (Hinsch 2002), and defocusing digital PIV (Pereira & Gharib 2002). Yet drawbacks of these techniques include the requirement of the scanning rate to be greater than the flow time scales of interest, complicated optical arrangements, as well as a limited seeding particle concentration, respectively. One of the most recent volumetric extensions of PIV, which arguably minimizes these limitations, as well as being suitable for application to high-speed flows, is tomographic PIV introduced by Elsinga *et al.* (2006). This technique determines the particle velocity field within a three-dimensional measurement volume based on the simultaneous view of illuminated particles by digital cameras placed along several different viewing directions. While the initial applications of tomographic PIV have been performed in low-speed, low-Reynolds-number flows (see Schröder *et al.* 2007; Elsinga *et al.* 2007*b*), its extension to the supersonic flow regime has been recently achieved by Elsinga *et al.* (2007*a*), and makes the application of tomographic PIV to the SWTBLI problem well-posed. The present paper describes the first experimental study to obtain volumetric information on the three-dimensional instantaneous structure of a SWTBLI. In what follows, the working principles of tomographic PIV are outlined in § 2. The experimental procedure is described in § 3 and the results are presented in § 4. A summary and discussion is given in § 5, followed by conclusions in § 6.

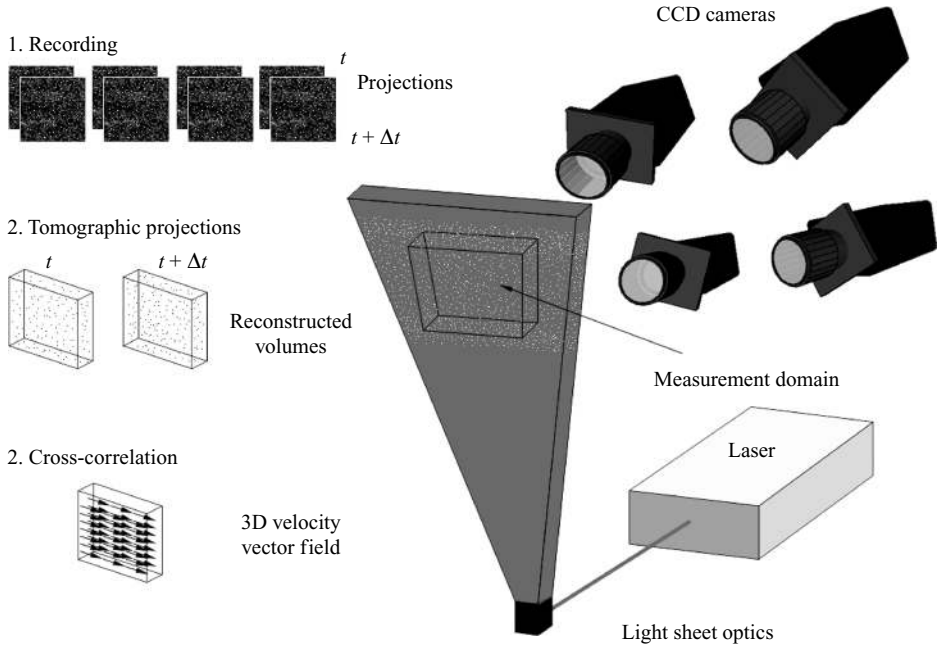

FIGURE 1. A schematic of the working principles of tomographic PIV. The procedure includes illuminating the flow with a laser and recording image projections by several CCD cameras. The projections are then reconstructed as three-dimensional particle distributions, which are then cross-correlated to give a volumetric velocity vector field. The schematic is based on Elsinga *et al.* (2006).

2. Working principles of tomographic PIV

Tomographic PIV is based on the principles of optical tomography, which essentially reconstructs a three-dimensional volume (the object) on the basis of a set of simultaneous images taken from different viewing directions. A detailed discussion of the principles and implementation of the technique is given by Elsinga *et al.* (2006). Briefly, tracer particles are illuminated within a measurement volume by a pulsed light source, as shown in figure 1. The scattered light is captured simultaneously from several different viewing directions by a series of charge couple device (CCD) cameras. The object is then reconstructed as a three-dimensional light intensity distribution using the multiplicative algebraic reconstruction technique (MART) (see Herman & Lent 1976).

In the present approach, the object is represented in discretized form, as a three-dimensional array of cubic voxel elements, and the set of linear equations, which model the imaging system, are solved iteratively. The object is given by a series of three-dimensional voxels in physical space (X, Y, Z), with the light intensity given by $E(X, Y, Z)$. The projection of the light intensity distribution onto each image pixel (x_i, y_i) gives the image intensity distribution $I(x_i, y_i)$, for each viewing direction. The system of equations relating E and I is given by

$$\sum_{j \in N_i} w_{i,j} E(X_j, Y_j, Z_j) = I(x_i, y_i) \tag{1}$$

where $w_{i,j}$ is the weighting coefficient that describes the contribution of the jth voxel intensity $E(X_j, Y_j, Z_j)$ to the ith pixel intensity $I(x_i, y_i)$. N_i is the total number

of voxels in the line-of-sight corresponding to the ith pixel (x_i, y_i). In practice, the MART is implemented as an iterative technique, with the update of the system of equations based on the ratio between the measured pixel intensity and the projection of the object, along with an appropriate scalar relaxation parameter. The iterative object update is

$$E^{k+1}(X_j, Y_j, Z_j) = E^k(X_j, Y_j, Z_j) \left[I(x_i, y_i) \Big/ \sum_{j \in N_i} w_{i,j} E^k(X_j, Y_j, Z_j) \right]^{\mu w_{i,j}} \tag{2}$$

where μ is the scalar relaxation parameter, with the property that $\mu \in [0, 1]$. The magnitude of the update is therefore determined by the ratio of the measured pixel intensity $I(x_i, y_i)$ with the projection of the current object $E^k(X_j, Y_j, Z_j)$. The MART scheme requires that both E and I are positive definite. Furthermore, Elsinga *et al.* (2006) have shown that the accuracy of the tomographic reconstruction depends on a number of parameters including (i) the number of viewing cameras, (ii) the particle density present in the images, and (iii) to a lesser extent the angles between the viewing directions. The most commonly adopted configuration is four cameras with a seeding density of about 0.05 particles per pixel (p.p.p.), with viewing angles within the range 15° and 40° (see Elsinga *et al.* 2006).

Since accurate particle position reconstruction relies on the accurate triangulation of the camera views, the difference between the image coordinates and those within the reconstructed volume was established through a calibration procedure, similar to that followed in stereoscopic PIV, where a calibration target is recorded by each camera at several depth positions within the volume. This provided the different viewing directions and fields-of-view of each camera. The relationship between the physical and image coordinates is described by a third-order polynomial fit, as described by Soloff, Adrian & Liu (1997). Linear interpolation was used to find the corresponding image coordinates between the depth positions. After the acquisition of the recorded images during the experiment, a self-calibration procedure was then carried out, which allowed the above-mentioned triangulation to be corrected to a residual disparity below 0.2 pixels (see Wieneke 2007). The three-dimensional particle velocity was finally determined by a three-dimensional cross-correlation of the reconstructed particle distributions. As also noted by Elsinga (2008), the self-calibration procedure was found to slightly increase the returned vorticity levels, but does not affect the appearance of the flow structures to be discussed.

3. Experimental facility and procedure

3.1. *Flow facility*

Experiments were performed in the blow-down transonic-supersonic wind-tunnel (TST-27) of the High-Speed Aerodynamics Laboratories at Delft University of Technology. The facility generates flows in the Mach number range 0.5–4.2. The Mach number can be set by means of a continuous variation of the throat section and flexible nozzle walls. The tunnel operates at unit Reynolds numbers typically ranging from 30×10^6 to $130 \times 10^6\,\mathrm{m}^{-1}$, enabling an operating use of approximately 300 s. The maximum test-section dimensions are $270(H) \times 280(W)\,\mathrm{mm}^2$. In the present study, the tunnel was operated to match, within experimental uncertainty, the conditions of a previous planar PIV experiment of a very similar interaction reported by Humble, Scarano & van Oudheusden (2007). The nominal free-stream Mach number was $M_\infty = 2.1$ (free-stream velocity $U_\infty = 510\,\mathrm{m\,s}^{-1}$), with a stagnation pressure

Parameter	Quantity
M_∞	2.1
U_∞, m s^{-1}	510
δ, mm	20
δ^*, mm	4.4
θ, mm	1.4
u_τ, m s^{-1}	19.4
C_f	1.5×10^{-3}
P_0, kPa	280
T_0, K	280
Re_δ	7.0×10^5
Re_θ	4.9×10^4
Re_τ	8600

TABLE 1. Experimental parameters.

of $P_0 = 280$ kPa and stagnation temperature of $T_0 = 280$ K. HWA measurements performed in the free stream of the test-section determined the turbulence intensity to be approximately 1 % U_∞.

The boundary layer developing along the sidewall was chosen as the test boundary layer in order to match the flow scales with the resolution capabilities of the measurement technique and to provide good optical access. The boundary layer developed for approximately 2 m along a smooth surface under nearly adiabatic flow conditions. On entering the test-section, the boundary layer thickness (99 % of U_∞) was $\delta = 20$ mm, with displacement thickness $\delta^* = 4.4$ mm, and momentum thickness $\theta = 1.4$ mm. A log-law fit in combination with the van Driest transformation was used to determine the skin friction coefficient, $C_f = 1.5 \times 10^{-3}$ corresponding to a friction velocity, $v_\tau = \sqrt{(\tau_w/\rho_w)} = 19.4$ m s^{-1}. The Reynolds number based on the undisturbed boundary layer thickness, $Re_\delta = U_\infty \delta/\nu_\infty = 7.0 \times 10^5$ (where ν_∞ is the kinematic viscosity in the free stream), based on the momentum thickness, $Re_\theta = U_\infty \theta/\nu_\infty = 4.9 \times 10^4$, and based on the friction velocity and boundary layer thickness, $Re_\tau = u_\tau \delta/\nu_w = 8600$ (where ν_w is the kinematic viscosity at the wall). The experimental parameters are summarized in table 1. Mean flow properties and turbulence statistics of a very similar interaction obtained with planar PIV have been reported by Humble *et al.* (2007).

3.2. *Experimental arrangement*

A 70 mm chord shock generator imposing a deflection angle of 10° was placed in the free-stream flow to generate the incident shock wave. The generator was mounted vertically in the centre of the test-section on an 80 cm long sting and spanned 65 % of the test-section height. A schematic representation of the experimental arrangement is shown in figure 2. Note that the sting has been omitted for clarity. The origin of the coordinate system used in the present study is shown, with x measured in the downstream flow direction from the extrapolated wall-impingement location of the incident shock wave, y in the spanwise direction, and z in the wall-normal direction. For the distance chosen from the wall, the chord of the shock generator was sufficient to prevent the expansion fan at its shoulder from influencing the measurement domain. This configuration was also considered advantageous for the digital imaging of high-speed compressible boundary layers, since the density gradient ($\rho_w/\rho_e \approx 0.6$ at $M_e = 2.1$, where w and e denote the wall and boundary layer edge conditions,

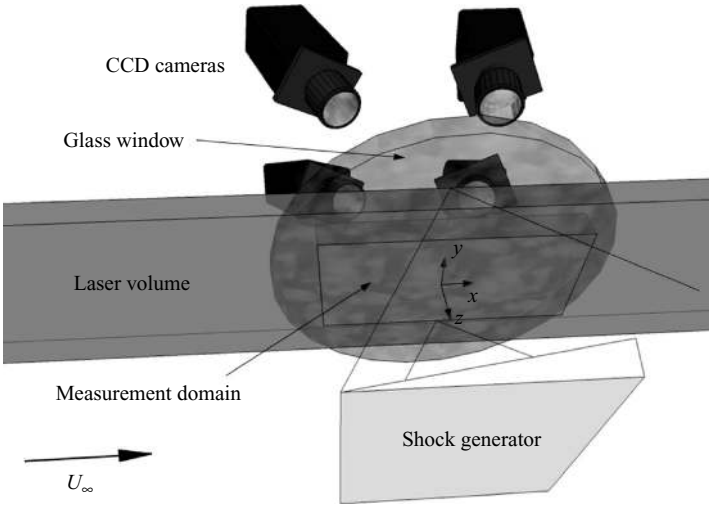

FIGURE 2. Schematic of the tomographic PIV experimental arrangement. Note that the sting has been omitted for clarity. Flow is from left to right.

respectively) was parallel with the viewing direction. This arrangement has been shown by Elsinga, van Oudheusden & Scarano (2005) to minimize the aero-optical distortion effects associated with PIV.

3.3. *Particle image velocimetry (PIV)*

Flow seeding and illumination constitute critical aspects of PIV in high-speed flows. A 10 mm diameter pipe was inserted into the settling chamber to seed the upstream boundary layer. Kemira-300 titanium dioxide (TiO_2) particles with a manufacturer-specified nominal diameter of 170 nm and a bulk density of 200 kg m^{-3} were adopted as tracers. The flow was seeded to an average concentration of 2 particles mm^{-1} (16 particles per interrogation box). The average particle image density was approximately 0.05 p.p.p., which has been shown to be sufficient to give an accurate particle reconstruction in the tomographic PIV technique (see Elsinga *et al.* 2006). The particle relaxation time across the incident shock wave has been previously estimated to be $\tau_p \approx 2.3\,\mu$s, corresponding to a frequency response $f_p \sim 450$ kHz (Schrijer & Scarano 2007). The effective (agglomerated) particle diameter has been estimated from electron microscopy scans of the porous agglomerates and found to be $d_p \sim 400$ nm (see Schrijer, Scarano & van Oudheusden 2006). As suggested by Samimy & Lele (1991), the particle dynamic effects may be further parameterized by the Stokes number, $St = \tau_p/\tau_f$ (where τ_f is taken to be the characteristic outer-flow time scale δ/U_∞). For accurate flow tracking at the time scale of τ_f, it is necessary to meet the criterion that $St \ll 1$. The corresponding Stokes number in the present experiments (based on $\delta/U_\infty \approx 40\,\mu$s) is about 0.06, indicating that the chosen particles track the flow with fidelity at the time scale of τ_f.

The seeded flow was illuminated by a Spectra-Physics Quanta Ray double-pulsed Nd:Yag laser, with 400 mJ pulsed energy and a 6 ns pulse duration at wavelength 532 nm. Laser light access into the test-section was provided by a laser probe inserted downstream of the test-section, with the light beam shaped into a volume using light optics. Because of the illumination close to the wall, a knife-edge slit filter was used before light entered the probe to remove the low-energy fringes present, and to give a better approximation of a top-hat light intensity distribution. This confinement of the

Parameter	Quantity
Interrogation volume	$2.1 \times 2.1 \times 2.1\,\mathrm{mm}^3$
Digital imaging resolution	≈ 23 pixels mm^{-1}
Objective focal length	$f = 60\,\mathrm{mm}$
f-number	$2 \times f_{\#} = 8, 2 \times f_{\#} = 11$
Laser pulse separation	$2\,\mu\mathrm{s}$
Seeding density	0.05 p.p.p.

TABLE 2. Summary of the tomographic PIV recording parameters.

illuminated region also facilitated the tomographic reconstruction phase. The laser pulse separation was set at 2 μs, which allowed a particle displacement in the free stream of approximately 1 mm (≈20 voxels).

Particle images were recorded by four LaVision Imager Pro X CCD cameras with a 2048×2048 14 bit pixel-sized sensor. Only 1216 pixels were used in the spanwise direction of the interaction given the aspect ratio of the flow region investigated. At the same time, this enabled a recording rate of 10 Hz. The flow was imaged in the streamwise (x), spanwise (y), and wall-normal (z) directions over a volume of approximately $70 \times 40 \times 10\,\mathrm{mm}^3$ ($3.5\delta \times 2\delta \times 0.5\delta$), respectively, with a digital imaging resolution of approximately 23 pixels mm^{-1}. The solid angle enclosed between all four cameras was $40^\circ \times 35^\circ$ in the streamwise–wall-normal and spanwise–wall-normal planes, respectively. Each camera was equipped with a Nikon 60 mm focal objective, with Scheimpflug adapters to place the focal plane in the mid-section of the measurement volume and so maintain the entire measurement domain in focus. The objectives were equipped with a narrow-bandpass 532 nm filter to minimize ambient light interference. The two cameras in forward-scatter had f-number $f_{\#} = 11$, and the two cameras in back-scatter had f-number $f_{\#} = 8$. The tomographic PIV recording parameters are summarized in table 2. Synchronization between the cameras, laser, and image acquisition was accomplished by an LaVision programmable timing unit controlled through DaVis 7.3 software, which was also used in the data recording, volume calibration, self-calibration, reconstruction, and three-dimensional cross-correlation based interrogation that yielded the velocity vector fields.

In view of a boundary layer thickness of 20 mm, the tomographic field-of-view extends over only half of the boundary layer thickness. Experiments were therefore performed in two regions, characterizing the lower and upper parts of the interaction, which are described in table 3. This was accomplished by translating both the laser probe and camera system. Reconstructed volumes were discretized at 20^3 voxels per mm^3. The particle images were interrogated using windows of final size $42 \times 42 \times 42$ voxels with an overlap factor of 75 %, resulting in a vector spacing of about 0.5 mm (0.03δ) in each direction. A dataset of order 200 velocity vector volumes was acquired in each region.

Particle images were preprocessed before volume reconstruction. This involved subtracting the time-minimum background intensity, as well as a sliding spatial minimum using a kernel of 51 pixels. Gaussian smoothing using a 3×3 kernel was then applied to reduce image noise. Post-processing involved identifying erroneous vectors using the universal median test (see Westerweel & Scarano 2005) with a maximum median deviation set at 2.5. The number of spurious vectors in the complete dataset was less than 5 %. These were removed, and replaced using a

	Δx (mm)	Δy (mm)	z-range (mm)	Vector grid size (x, y, z)	Vector spacing (mm)
Lower region	75 (3.8δ)	40 (2.0δ)	2–12 (0.1–0.6δ)	$141 \times 74 \times 22$	0.54 (0.03δ)
Upper region	69 (3.5δ)	42 (2.1δ)	12–20 (0.6–1.0δ)	$130 \times 79 \times 20$	0.53 (0.03δ)

TABLE 3. Description of the tomographic PIV measurement regions.

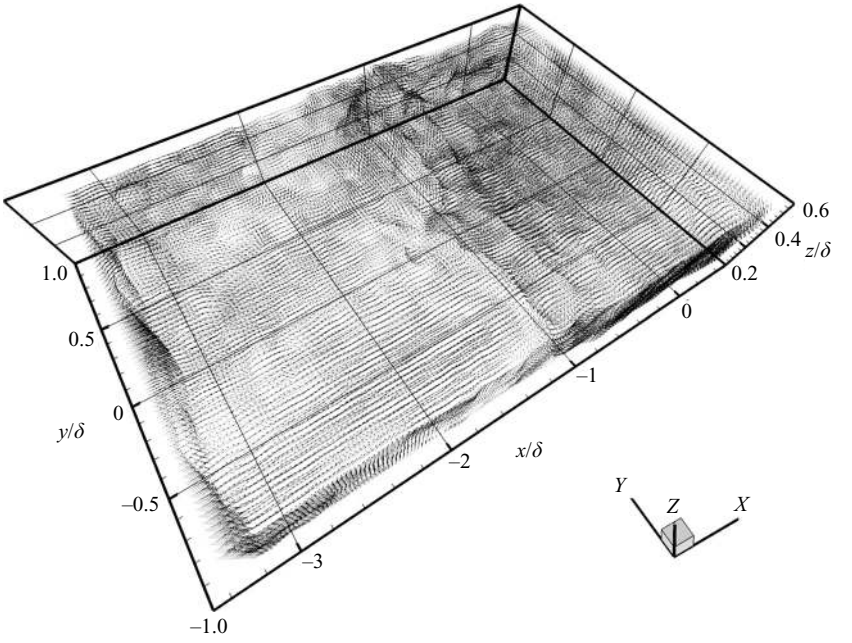

FIGURE 3. An example of the velocity vector distribution within the interaction: lower region ($z/\delta = 0.1$–0.6). Vectors are shown in a convective reference frame of $0.8U_\infty$. Only vectors at the boundaries of the measurement domain are displayed for clarity.

linear interpolation scheme. To ease visualization, the instantaneous velocity fields were filtered using a three-dimensional Gaussian filter based on a kernel of $3 \times 3 \times 3$ points. The average cross-correlation signal-to-noise ratio, defined as the ratio of the first and second correlation peak, was approximately 2.5 throughout the measurement domain. To give a first impression of the results, an example of a typical velocity vector field obtained in the lower region of the interaction is shown in figure 3. Vectors are shown in a convective frame of reference of $0.8U_\infty$ and only vectors at the boundaries of the measurement domain are displayed for clarity.

3.4. *Comparison with other experimental results*

In order to substantiate the validity of the present data, the tomographic PIV streamwise and wall-normal root-mean-square (RMS) velocity components within the undisturbed boundary layer, denoted by $\sqrt{\overline{u'^2}}$ and $\sqrt{\overline{w'^2}}$, respectively, are compared with the planar PIV results of Humble *et al.* (2007) and Hou (2003), the HWA and laser Doppler anemometry (LDA) results of Elena & Lacharme (1988), as well as

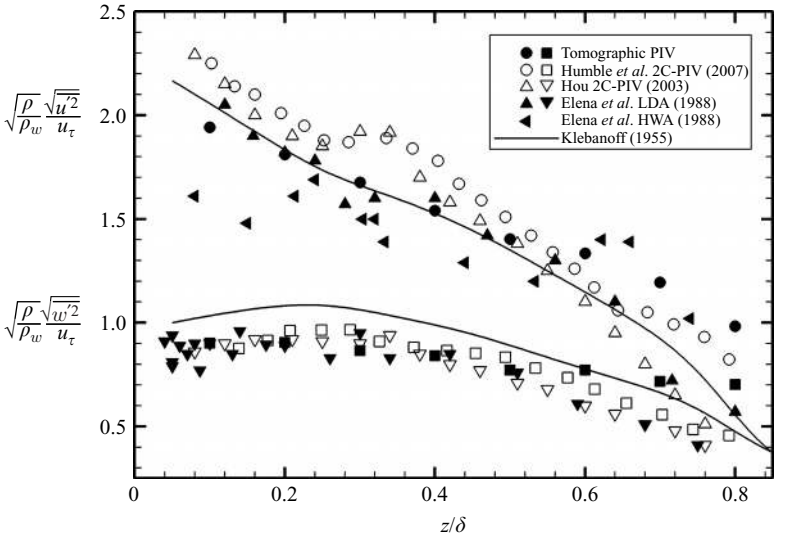

FIGURE 4. Comparison of the streamwise and wall-normal RMS velocity components within the compressible turbulent boundary layer using Morkovin's scaling. The present tomographic PIV results are compared with the experimental data of Humble *et al.* (2007), Hou (2003), Elena & Lacharme (1988) and Klebanoff (1955).

the incompressible results of Klebanoff (1955). These data are presented in figure 4, normalized by the friction velocity. In addition, Morkovin's hypothesis is used to take into account the density variation in the scaling by premultiplying the data with the density transformation $\sqrt{\rho/\rho_w}$, enabling a comparison to be made with the incompressible data of Klebanoff (1955). The local mean density was deduced from the mean velocity distribution using the adiabatic Crocco–Busemann relation with a constant recovery factor $r = 0.89$, with the assumption that the mean static pressure in the wall-normal direction remains constant. The present results can be seen to agree well with previous planar PIV measurements made within the present boundary layer, as well as with the other experimental results shown, substantiating the validity of the present data.

4. Results and discussion

4.1. *Basic features of the interaction*

To first provide an overview of the basic features of the interaction, figure 5 shows a short-exposure Schlieren visualization. Because the Schlieren image represents a spanwise average of the density gradients, there is relatively little indication of the large-scale structure within the incoming boundary layer. The penetration of the incident shock wave into the boundary layer can be readily observed. Except for the part within the boundary layer, the incident shock wave appears quite uniform in the spanwise direction. The dashed line represents the extrapolation of the incident shock wave to the wall, which is the origin of the coordinate system used. Compression waves form ahead of where the incident shock wave would impinge on the wall in the absence of the boundary layer. The comparatively high Reynolds number of the present experiments means that these compression waves emanate from relatively deep within the boundary layer. This upstream effect is consistent with the filtered

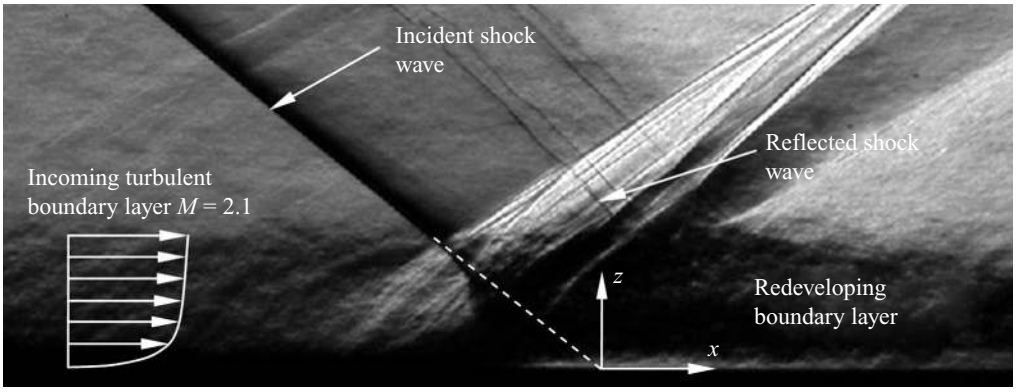

FIGURE 5. Short-exposure Schlieren visualization of the interaction. Origin of coordinate system is located at the extrapolated wall-impingement point of the incident shock wave.

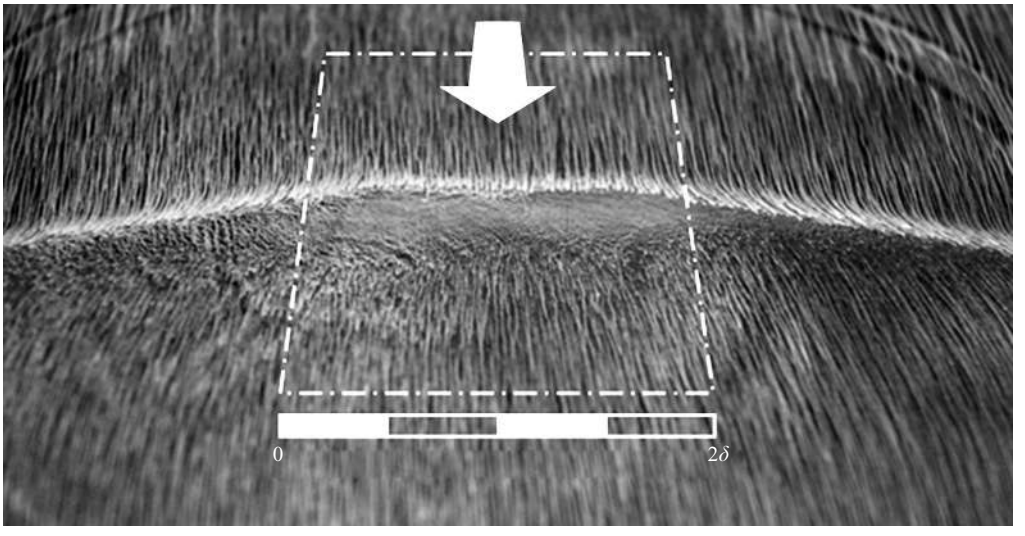

FIGURE 6. Surface oil flow visualization of the interaction. The flow direction is from top to bottom as indicated by the white arrow. The figure is shown in a perspective view. The (projected) measurement domain is indicated by the dashed box.

Rayleigh scattering visualizations of an incident SWTBLI by Bookey, Wyckham & Smits (2005). The compression waves coalesce as they leave the boundary layer to form the reflected shock wave. A significant distortion of the reflected shock wave can be observed in the spanwise direction, which will become a focal point of our discussion later on. Farther downstream, the redeveloping boundary layer undergoes a recovery process.

To assess possible spanwise non-uniformities that are often present in such nominally two-dimensional interactions, figure 6 shows a surface oil flow visualization of the interaction. The flow direction is from top to bottom and is shown in a perspective view. The (projected) measurement domain is indicated by the dashed box. It is evident that the interaction remains largely symmetric about the centreline within the spanwise region considered. For distances greater than δ from the centreline, however, appreciable three-dimensional effects may be observed, which are attributed

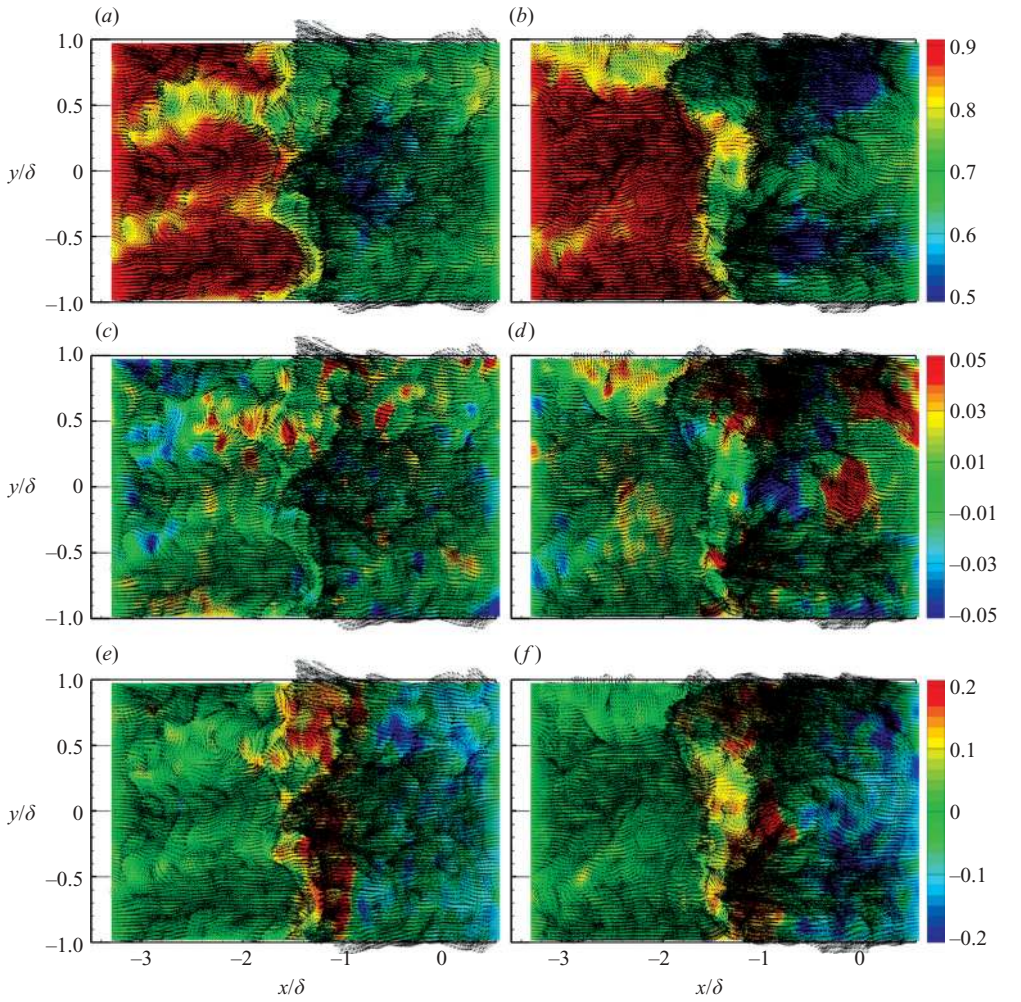

FIGURE 7. Cross-sectional representations of the instantaneous flow organization of the interaction. Results show instantaneous velocity distributions at $z/\delta = 0.12$ extracted from the tomographic PIV measurement volumes. Two uncorrelated realizations for each velocity component are displayed on the left and right, respectively. (a, b) instantaneous streamwise velocity u/U_∞, (c, d) instantaneous spanwise velocity v/U_∞, (e, f) instantaneous wall-normal velocity w/U_∞.

to the limited span of the shock generator. The mean velocity components obtained by planar PIV also show a similar spanwise uniformity within the present measurement domain (see Humble *et al.* 2007).

4.2. *Cross-sectional representation of the instantaneous flow organization of the interaction*

As the motivating prelude to the volumetric results, cross-sectional velocity fields are extracted from the tomographic PIV measurement volumes relatively close to the wall at $z/\delta = 0.12$ and are presented in figure 7. Two uncorrelated instantaneous velocity distributions of the interaction are displayed, on the left and right, respectively, representing the colour-coded instantaneous streamwise (u/U_∞), spanwise (v/U_∞),

and wall-normal (w/U_∞) velocity components. Each field is over-laid with in-plane instantaneous velocity vectors shown in a convective frame of reference of $0.8U_\infty$ in the streamwise direction. These results have been chosen because they exemplify the typical flow features observed.

The results capture the incoming boundary, as well as the reflected shock wave region, the latter initiating at approximately $x/\delta = -1.5$ (see e.g. figure 7*a*). The redeveloping boundary layer is observed farther downstream. Even in this cross-sectional representation, the interaction appears highly unsteady and complex. The instantaneous streamwise velocity distribution shown in figure 7(*a*) portrays distinct, large-scale regions containing low- and high-speed fluid within the incoming boundary layer, which are parallel to the wall, and elongated in the streamwise direction. Relatively large velocity differences of up to $100\,\mathrm{m\,s^{-1}}$ ($0.2U_\infty$) occur between these low- and high-speed regions, consistent with the observations made by Ganapathisubramani *et al.* (2006), who carried out planar PIV measurements in a supersonic turbulent boundary layer at Mach 2 and $z/\delta = 0.16$.

Because of the limited size of both the present measurement domain and a number of measurement volumes, it is not possible to accurately determine their characteristic geometry (in particular, their streamwise length). However, they appear to have a streamwise extent of at least 2δ based on the present measurement domain. Ganapathisubramani *et al.* (2007) report lengths of up to 40δ using planar laser scattering (PLS) and Taylor's hypothesis in their Mach 2 boundary layer. Such long low- and high-speed regions have also been reported in compressible boundary layers by many other authors, such as Samimy *et al.* (1994), Ganapathisubramani *et al.* (2006), Elsinga *et al.* (2007), and Ringuette *et al.* (2008) for instance, as well as in incompressible boundary layers by Kim & Adrian (1999), Hutchins & Marusic (2007), Tomkins & Adrian (2003) and Ganapathisubramani, Longmire & Marusic (2003). On the other hand, these streamwise-elongated regions are not ubiquitous in the present data. For instance, figure 7(*b*) shows a relatively high-speed region that appears to span almost the measurement domain.

The streamwise-elongated regions when they occur appear to have a limited spanwise extent. Figure 7(*a*) suggests that the spanwise dimensions of the low-speed regions are typically within the range $\Delta y = 4$–$10\,\mathrm{mm}$ (0.2–0.5δ), as confirmed by the statistical analysis performed by Elsinga *et al.* (2007) in the undisturbed boundary layer of the present study. These results are also consistent with what has been reported in other supersonic boundary layers, such as the range 0.25–0.5δ reported by Ganapathisubramani *et al.* (2006) at $z/\delta = 0.16$, the range 0.4–0.5δ reported by Spina, Donovan & Smits (1991) using two-point correlations, as well as the DNS computations of Ringuette *et al.* (2008) who report about 0.5δ. It is important to remark that the spatial organization of these regions disappears after data averaging, indicating that they are not stationary features.

The corresponding instantaneous spanwise velocity distributions are shown in figure 7(*c*, *d*). Note that the spanwise velocity range is smaller than for the other velocity components. The spanwise velocity component appears much less coherent along both the streamwise and spanwise directions in comparison to the streamwise component, consistent with the two-point correlations made by Ganapathisubramani *et al.* (2005) in their incompressible turbulent boundary layer. A comparison between figures 7(*a*) and 7(*c*) indicates that the spatially compact regions of spanwise velocity are typically observed within the streamwise-elongated low-speed regions. Figure 7(*c*) shows that the spanwise velocity regions persist throughout the interaction, whereas figure 7(*d*) shows an increase in both the magnitude and spatial extent of these

regions. It is therefore often difficult to determine the compression region from the spanwise velocity distributions alone.

The corresponding wall-normal velocity distributions are shown in figure 7(e, f). Relatively small fluctuations can be observed within the incoming boundary layer. In contrast, relatively large positive fluctuations of the order of $100\,\mathrm{m\,s^{-1}}$ ($0.2U_\infty$) can be observed within the compression region, associated with the dilatation of the subsonic fluid in this part of the interaction. Farther downstream, the redeveloping boundary layer becomes populated with spatially compact regions of negative wall-normal velocity, consistent with the formation of a mixing-type layer, as observed by Pirozzoli & Grasso (2006) in their DNS of an incident SWTBLI.

4.3. *Volumetric representation of the instantaneous flow organization of the interaction: lower region* ($z/\delta = 0.1$–0.6)

The main results of this paper are now presented. A series of uncorrelated volumetric representations of the interaction's instantaneous flow organization are shown in figure 8, obtained in the lower region of the interaction ($z/\delta = 0.1$–0.6). Note that figure 8(a, b) corresponds to figure 7(a, b). For the purposes of illustration, three values of streamwise velocity isosurface are displayed in each volume: high-speed in red ($0.9U_\infty$), intermediate velocity in green ($0.75U_\infty$), and low-speed in blue ($0.55U_\infty$). Velocity vectors in the streamwise–wall-normal plane are shown coloured with instantaneous streamwise velocity.

Figure 8(a) shows that the relatively low- and high-speed regions observed in the cross-sectional results are in fact highly three-dimensional, with widths that vary in the wall-normal direction. This phenomenology is consistent with the DNS of Ringuette *et al.* (2008), who viewed regions of relatively low-speed fluid using velocity isosurfaces, and also found them to be highly three-dimensional, interpreting them as chains of bulges. Figure 8(b) shows that the widths of the high-speed regions also vary in the streamwise direction. In this particular case, such regions appear interconnected, although this is more likely to be associated with the termination of the low-speed region in between. The closing pattern of the isosurface around this feature suggests that it does not extend much farther than the edge of the measurement domain ($z/\delta = 0.6$), and is therefore embedded within the lower part of the incoming boundary layer. A volumetric representation therefore reduces the complexity and ambiguity of the cross-sectional results, by providing a volumetric synthesis of such an observation, as recognized by Delo, Kelso & Smits (2004) in their three-dimensional visualizations of the instantaneous structure of a turbulent boundary layer.

Instantaneous velocity isosurfaces are used to make inferential statements regarding the overall reflected shock wave pattern at this height within the boundary layer, similar to the approach carried out by Ganapathisubramani *et al.* (2007) in their compression ramp interaction; they computed a surrogate for the instantaneous separation point using a velocity threshold criterion. Figure 8(a, b) shows that the reflected shock wave region undergoes spanwise undulations of the order of 0.5δ (see also the statistical analysis in § 4.6), whereas figure 8(c) shows a relatively uniform reflected shock wave region that is displaced in the streamwise direction. These two types of configuration are rather ubiquitous throughout the dataset. Wu & Martin (2008) have carried out a DNS of a compression ramp interaction, and using contours of pressure gradient magnitude in streamwise–spanwise planes observed that the streamwise movement of the shock wave was about δ, with a wrinkling in the spanwise direction of about 0.5δ. It appears that the instantaneous spatial

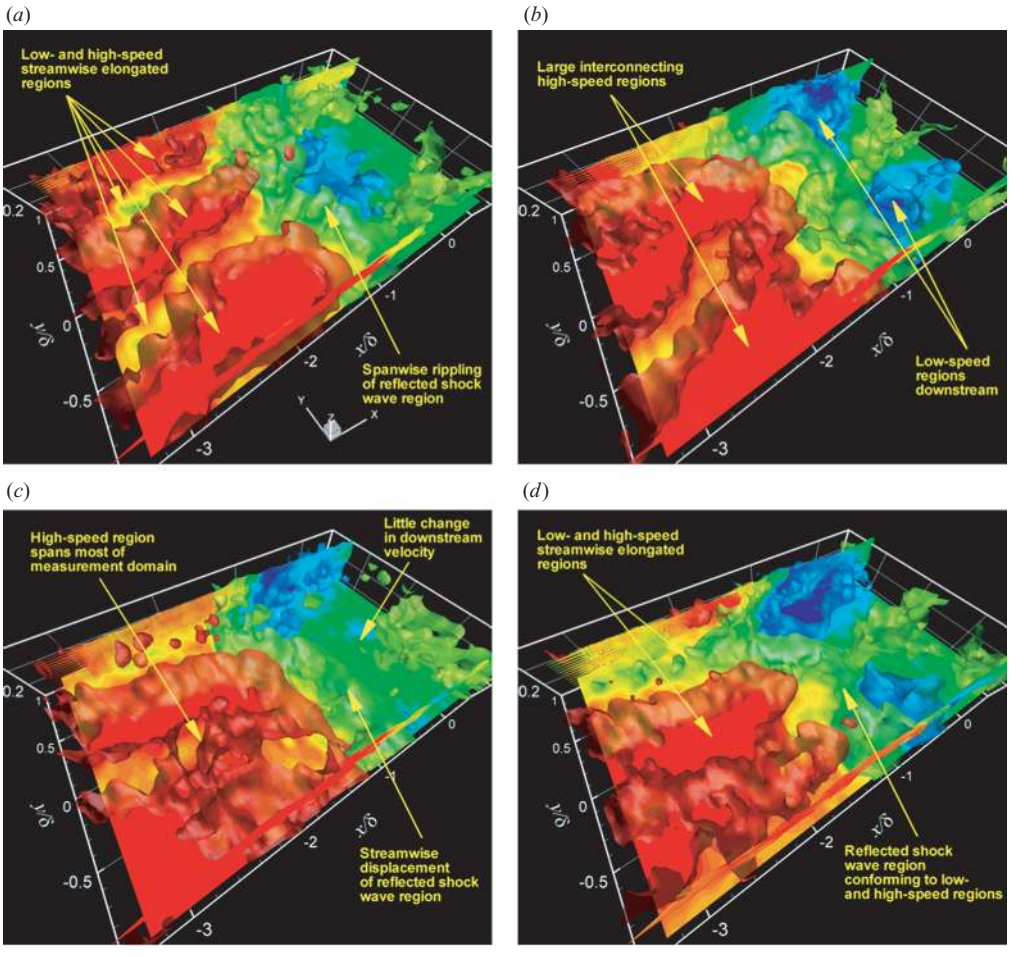

FIGURE 8. Volumetric representations of the instantaneous flow organization of the interaction: lower region ($z/\delta = 0.1$–0.6). Isosurfaces of streamwise velocity are shown: relatively high-speed in red ($0.9U_\infty$), intermediate velocity in green ($0.75U_\infty$), and relatively low-speed in blue ($0.55U_\infty$). Velocity vectors are shown flooded with instantaneous streamwise velocity. (a, b) correspond to figure 7 (a, b).

organization of the present reflected shock wave region may also be characterized as a superposition of streamwise translation and spanwise rippling patterns, as proposed by Wu & Martin (2008).

Closer inspection of the results reveals that these patterns are associated with the spatial organization of the incoming boundary layer. Figure 8(a, b, d) exemplifies the observation that a relatively high-speed region entering the interaction corresponds to a reflected shock wave region that is relatively downstream, whereas a relatively low-speed region entering the interaction corresponds to a reflected shock wave region that is relatively upstream. The reflected shock wave pattern therefore appears to conform to the low- and high-speed streamwise-elongated regions within the incoming boundary layer as they enter the interaction, in agreement with the study by Ganapathisubramani *et al.* (2007), who observed that the separation region conforms to very long regions of alternating low- and high-speed fluid within the

logarithmic region of the incoming boundary layer. It therefore seems that the large-scale unsteadiness of incident shock wave and compression ramp interactions share some important physical features.

4.4. *Vorticity organization*

To further characterize the unsteady flow organization of the interaction, regions of vorticity magnitude are visualized. Although the present resolution is insufficient to permit a quantitative study of the vorticity characteristics, the results may be used qualitatively to highlight the overall vortex organization. Figure 9 presents an artistic overview of the main phenomenological features of the interaction using the measurement volume of figure 8(*a*), chosen because it embodies several key elements that are characteristic of the ensemble of data. Semitransparent isosurfaces of vorticity magnitude $|\boldsymbol{\omega}| = \sqrt{\omega_x^2 + \omega_y^2 + \omega_z^2}$ are shown for $|\boldsymbol{\omega}|\delta/U_\infty = 1.0$, determined using central-differencing. Also shown in the figure are velocity vectors in a convective frame of reference of $0.8U_\infty$, complemented with flooded streamwise velocity contours in the streamwise–spanwise plane.

The results portray an incoming boundary layer with a rich, instantaneous structure, populated with numerous regions of concentrated vorticity of various shapes and sizes. While in previous planar PIV measurements, discrete, disconnected regions of vorticity have been identified (see e.g. Adrian, Meinhart & Tomkins 2000; Tomkins & Adrian 2003; Ganapathisubramani *et al.* 2006), it is now clear that these regions are in fact connected out of the plane of the laser sheet in three-dimensional space, forming a complicated instantaneous flow structure. The present regions of vorticity often appear to form complex interconnected agglomerations, consistent with the observations made by Delo *et al.* (2004) in their three-dimensional visualizations of an incompressible boundary layer, and are most likely the remnants of the inclined vortex loops, horseshoes, or hairpin structures in the outer layer of the boundary layer, as described by Head & Bandyopadhyay (1981) and Adrian *et al.* (2000).

The observed structures typically appear in a quasi-streamwise alignment, in agreement with the observations made by numerous authors, such as Elsinga *et al.* (2007) and Ringuette *et al.* (2008) for instance. It is evident that such regions of vorticity typically occur within the low-speed regions and at the interface between the low- and high-speed regions. This is also consistent with the observations made by Elsinga *et al.* (2007) and Ringuette *et al.* (2008), who found that groups of hairpin packets were frequently located above the long low-momentum regions. These results thereby support the hairpin packet model reported by Kim & Adrian (1999), Adrian *et al.* (2000), Tomkins & Adrian (2003) and Ganapathisubramani *et al.* (2003) among many others, which explains the existence of the streamwise-elongated regions of uniform velocity extending to distances greater than 2δ, by asserting that the induced motion of several hairpins in streamwise alignment perpetuates the low- and high-speed regions.

In addition, it can be seen that very few structures occur within the high-speed regions, as shown in figure 9 (bottom left). Instead, the high-speed regions exhibit a three-dimensional spanwise sinuous or undulating motion, and appear to meander between the surrounding vortical structures. Such a scenario is consistent with a number of vortical structures that are in a spanwise-staggered array, an intriguing observation that has also been reported by Elsinga *et al.* (2007) using autocorrelations of wall-normal swirl strength in a plane parallel to the wall. Although not as widely

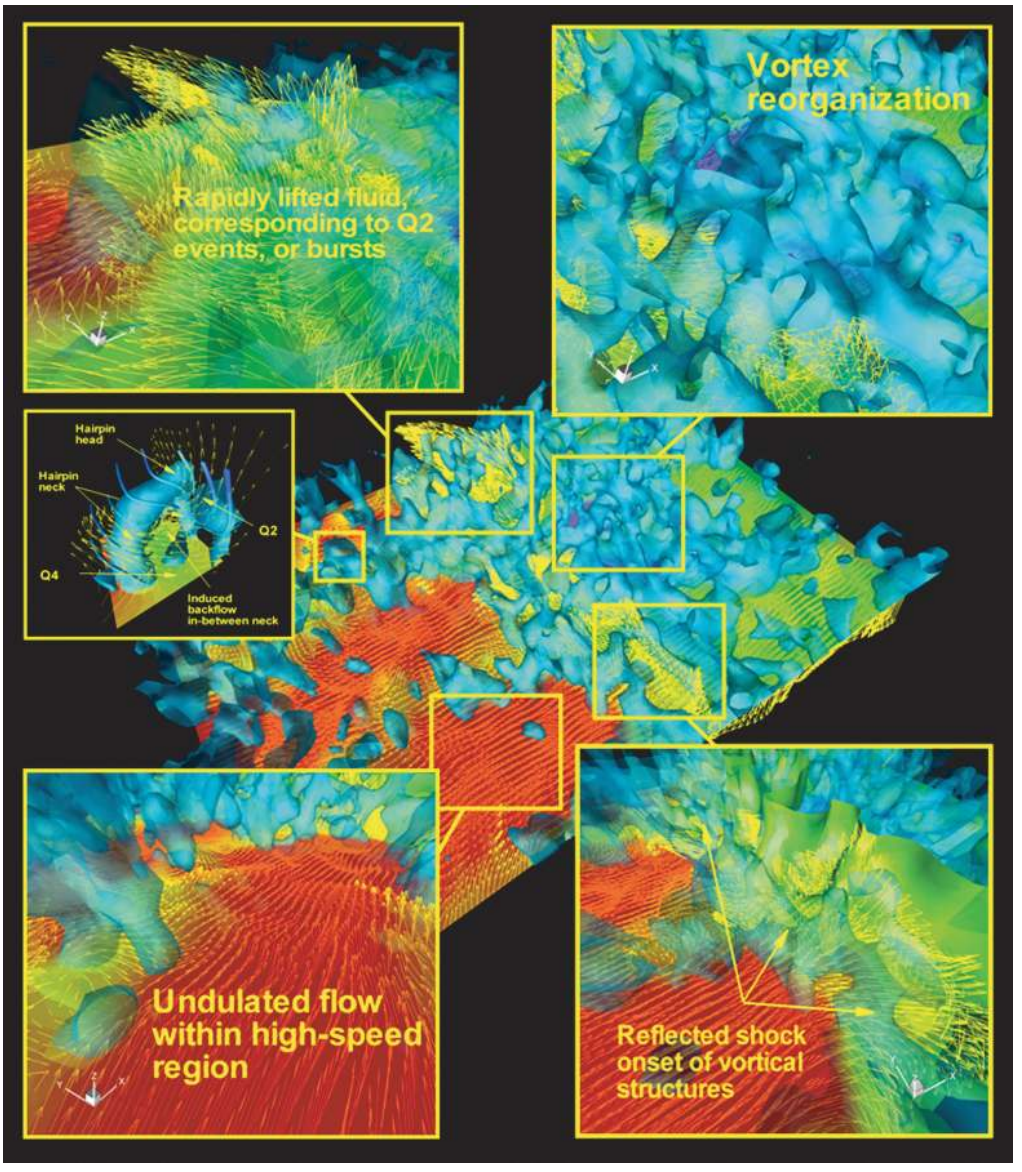

FIGURE 9. Overview of the main phenomenological features of the interaction: lower region ($z/\delta = 0.1$–0.6). Semitransparent vorticity isosurfaces for $|\boldsymbol{\omega}|\delta/U_\infty = 1.0$ are shown. Velocity vectors with a convective velocity of $0.8U_\infty$ are shown at $z/\delta = 0.26$ along with flooded streamwise velocity contours.

documented as some of their other characteristic features, such diagonal inclinations of vortical structures have also been reported by Delo *et al.* (2004).

Considered individually, there are many structures in the dataset that form arch, cane, and hairpin-type structures, as discussed by Adrian *et al.* (2000) among many others. For the purposes of illustration, one such structure is displayed in greater detail in figure 9 (middle left). It is approximately 0.3δ wide and 0.4δ high, and is convecting at around 80 % of U_∞. Elsinga *et al.* (2007) and Ringuette *et al.* (2008) have also

visualized a packet of such structures of similar geometric dimensions. The illustrated structure, however, is neither symmetric, nor identical to the other structures observed. While it is embedded within the surrounding turbulent environment, its imprint on the velocity field is clear: a spanwise vortex core can be seen located at its head, rotating in the same direction as the mean circulation. A region of backflow located below and slightly downstream of the head can be seen to be induced between its neck. Relatively faster moving fluid can be seen to be induced on the outboard portions of the hairpin's neck. Below and downstream of its head, there is a region of Q2 ($u' < 0$, $w' > 0$) events opposed by a region of Q4 ($u' > 0$, $w' < 0$) events, although no stagnation point can be unambiguously identified. Remarkably, ejected fluid extends from relatively close to the wall ($z/\delta \approx 0.1$), well into the outer part of the boundary layer ($z/\delta > 0.6$), representing a significant fluid exchange. The fact that it takes place within the incoming boundary layer suggests that it is already quite active as it approaches the interaction. Streamlines of locally induced flow indicate a swirling pattern around the necks and head, and confirm an overall circulation around the hairpin. The correspondence between this swirling motion and the isosurface justifies the use of vorticity magnitude as an appropriate quantity for the visualization of vortical structures in this flow.

Figure 9 (top left) shows that as the interaction is approached, a large region containing Q2 events develops within the reflected shock wave region, as the outer supersonic fluid within the boundary layer is displaced due to the dilatation of the inner subsonic fluid. Planar PIV results by Humble *et al.* (2007) in the streamwise–wall-normal plane have shown that in this first part of the interaction, ejected fluid can penetrate a significant distance into the outer part of the boundary layer (often up to $z/\delta \approx 0.6$), while traversing only a relatively short streamwise distance. It is now clear, however, that this process is highly three-dimensional, with the ejection of fluid varying significantly across the span of the interaction. One can only speculate about the interaction between the Q2 events produced by the displacement of the supersonic flow, and the Q2 events produced by the hairpin structures as they propagate through the interaction. The complex, three-dimensional nature of the flow makes even the unambiguous detection of such a process extremely difficult. Nevertheless, we expect these types of behaviour to be a significant source of kinematic Reynolds shear stress, since any element of fluid with less than average u and positive w contributes to the Reynolds-averaged shear stress. Turbulence statistics of the interaction that show the reflected shock wave to be a region of explosive increase in Reynolds-averaged shear stress is a testament to this (see Humble *et al.* 2007).

Figure 9 (bottom right) shows that the reflected shock wave region is the nucleation site for the onset of vorticity across the span of the interaction. This is in agreement with the vorticity results obtained by Ganapathisubramani *et al.* (2007) in their compression ramp interaction, who report that the interaction acts like a vorticity amplifier. As the vortical structures propagate through the interaction, it appears that they undergo a significant spatial reorganization. Figure 9 (top right) shows that the structures typically lose their identity downstream, and develop approximately parallel, non-parallel, and orthogonal alignments, which occur in close proximity. They appear to concatenate with each other to form more complicated arrangements, whereas in other cases, they appear relatively isolated and disconnected. Wu & Martin (2007) also visualized vortical structures within their compression ramp interaction, and found that the structures became more chaotic and of smaller extent as a result of the interaction, attributing the latter observation to either the chopping of the structures by the shock wave, or due to their compression through the shock wave.

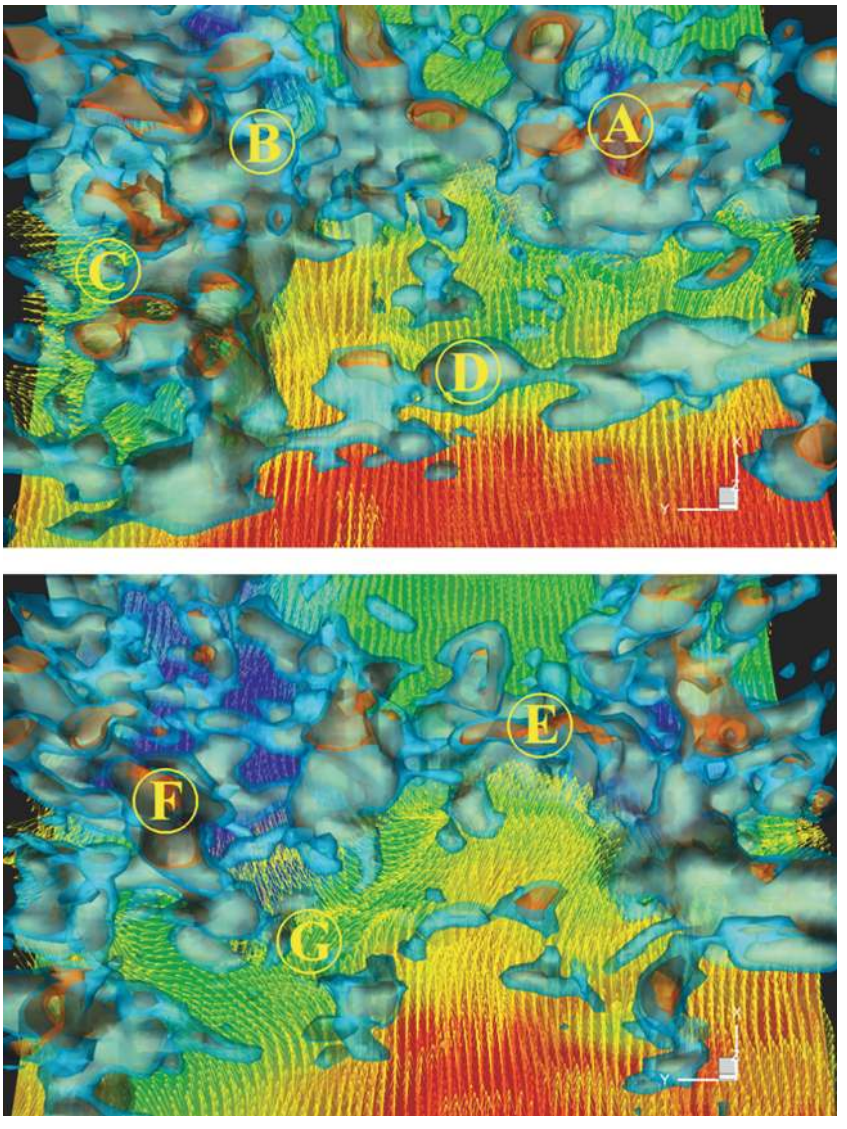

FIGURE 10. Two uncorrelated visualizations of the instantaneous vorticity organization of the interaction: lower region ($z/\delta = 0.1$–0.6). See figure 9 for visualization details. Flow is from bottom to top. Labelled regions are discussed in the text.

The interaction is examined in further detail in figure 10, which shows two uncorrelated visualizations of its instantaneous vorticity organization. Visualization details are the same as those used in figure 9, except that the vorticity magnitude isosurfaces have now been nucleated for clarity. It can be seen that there is quite some difference in the global vorticity organization within the interaction from instant to instant. The results confirm that the reflected shock wave region is the nucleation site for the onset of vorticity across the span of the interaction, beginning at the inception of the reflected shock wave region within the boundary layer. Region (D) illustrates a common observation in this dataset: that regions of relatively high vorticity often

appear as interconnected chains. These may well be the remnants of spanwise roller-type structures, as observed by Pirozzoli & Grasso (2006), who mention that they become important within the interaction zone.

Although difficult to discern from this representation, it appears that as the flow passes through the interaction, very few vortical structures are in contact with the wall. This is again consistent with the study of Pirozzoli & Grasso (2006), who attributed the onset of such structures to the formation of a mixing layer and its subsequent evolution, eventually leading to new structures farther downstream. The present results are also reminiscent of the DNS of incompressible separated flows by Na & Moin (1998) and Chong *et al.* (1998), who showed that vortical structures and the vorticity layer are lifted away from the wall in the first part of the separation process. Notice that many of the present structures, particularly those predominantly oriented normal to the wall, are cut in the streamwise–spanwise plane. This is due to the limited height of the measurement domain. This observation is particularly apparent within the redeveloping boundary layer, as shown in regions (A) and (F) for instance, and is consistent with the idea that an increase in vorticity occurs throughout the interaction zone.

The spatial organization of the incoming boundary layer appears to be associated with the instantaneous spanwise vorticity distribution. For example, regions (B) and (F) show a relatively large train of vortical structures persisting throughout the interaction, extending from a relatively low-speed region within the incoming boundary layer, well into the redeveloping boundary layer. In contrast, region (E) shows that a relatively high-speed region entering the interaction leads to a significant downstream displacement and distortion of a vorticity region in the streamwise direction. It therefore appears that the instantaneous vorticity organization is associated with the low- and high-speed regions within the incoming boundary layer, in much the same way as observed earlier for the velocity isosurfaces within the reflected shock wave region. Finally, it is interesting to observe how a significant spanwise flow tends to precede the low-speed regions within the incoming boundary layer, such as in regions (C) and (G) for instance. This is in contrast to what often precedes the high-speed regions (see to the left of (D) and upstream of (E)), where the flow appears to penetrate relatively deep into the reflected shock wave region with relatively little spanwise variation.

4.5. *Volumetric representation of the instantaneous flow organization of the interaction: upper region* ($z/\delta = 0.6$–1.0)

Moving farther away from the wall, a series of uncorrelated measurement volumes obtained in the upper region of the interaction are presented in figure 11. For the purposes of illustration, three values of streamwise velocity isosurface are again displayed: high-speed in red ($0.99U_\infty$), intermediate velocity in green ($0.85U_\infty$), and low-speed in blue ($0.75U_\infty$).

The results at this level within the interaction portray a rather different type of flow organization than observed closer to the wall. Although streamwise-elongated regions of relatively low-speed fluid can still be observed within the incoming boundary layer (e.g. figure 11*b*), such observations are not as common in this dataset. This is in agreement with the observations made by Ganapathisubramani *et al.* (2007), who obtained sequences of images of their compression ramp interaction using PLS at $z/\delta = 0.7$, and also found that the strips of uniform momentum in the upstream boundary layer were not as prevalent compared with their measurements closer to

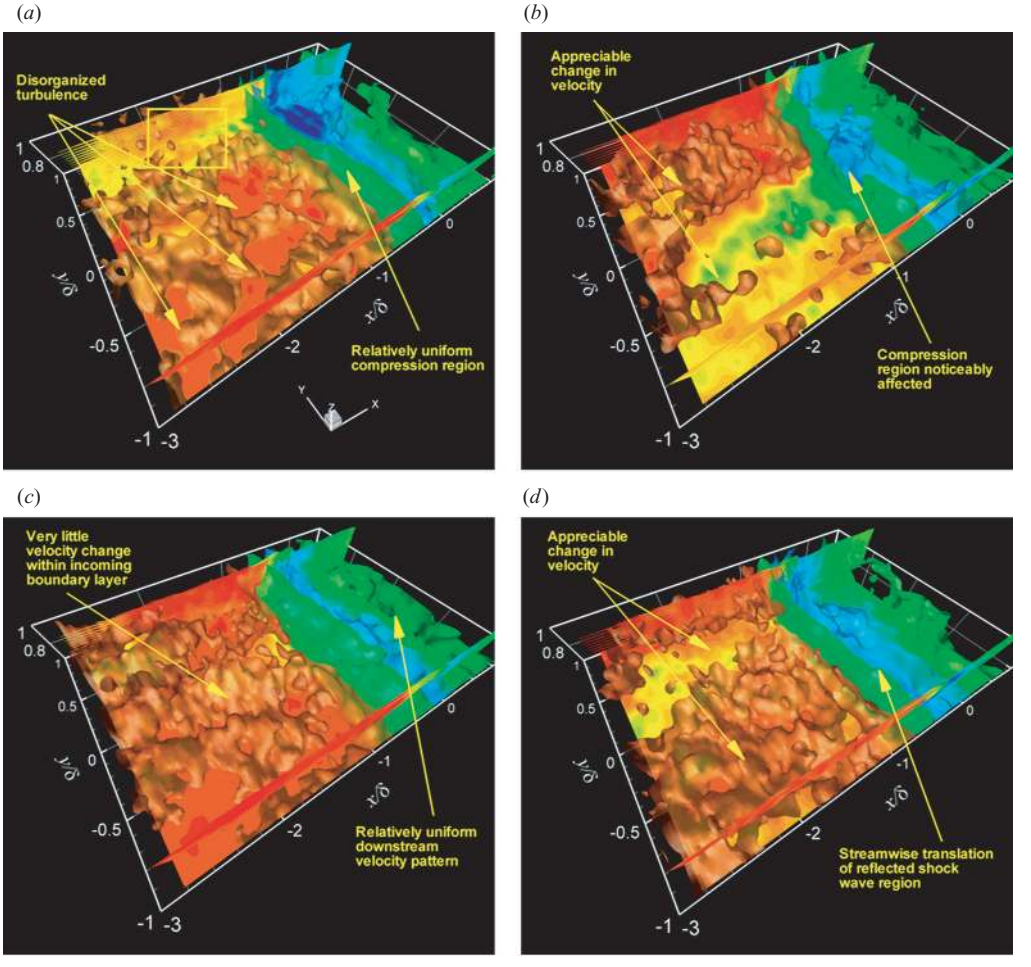

FIGURE 11. Volumetric representations of the instantaneous flow organization of the interaction: upper region ($z/\delta = 0.6$–1.0). Isosurfaces of streamwise velocity are shown: relatively high-speed in red ($0.99U_\infty$), intermediate velocity in green ($0.85U_\infty$), and relatively low-speed in blue ($0.75U_\infty$). Velocity vectors are shown flooded with instantaneous streamwise velocity. The subvolume indicated in (*a*) by the yellow box is rendered in greater detail in figure 12.

the wall. These authors still occasionally observed, however, long structures extending several boundary layer thicknesses in the streamwise direction.

In the present results, there is also evidence of a significant fluid exchange between the outer part of the boundary layer and the free-stream flow. Based on the high-speed isosurface ($0.99U_\infty$), it appears that at the boundary layer edge, the turbulent/non-turbulent interface may be characterized as a highly corrugated surface, consistent with the observations of Smith & Smits (1995), who visualized the structure of supersonic boundary layers using Schlieren and Rayleigh scattering, and characterized the outer layer as consisting of an array of regularly spaced uniform low-density bulges, separated from a uniform higher-density free stream by a sharp, instantaneously ragged interface. The average velocity inside the relatively high-vorticity regions in figure 11 is close to the free stream ($0.9U_\infty$), also consistent with observations of Smith & Smits (1995), who report that structures in the outer

FIGURE 12. Instantaneous flow structure of the incoming boundary layer: upper region ($z/\delta = 0.6$–1.0). Semitransparent vorticity magnitude isosurfaces for $|\boldsymbol{\omega}|\delta/U_\infty = 0.5$ are shown. Velocity vectors with a convective velocity of $0.8U_\infty$ are shown in two planes; at $y/\delta = 0.5$ and $z/\ \delta = 0.6$, the latter flooded with streamwise velocity contours. Streamlines are computed within this convective reference frame.

region convect at around $0.9U_\infty$. As a matter of fact, Spina *et al.* (1991) have shown that the convection velocity of the large-scale motions is nearly constant across 80 % of the supersonic boundary layer and is equal to approximately $0.9U_\infty$.

To illustrate more clearly some typical instantaneous flow structure in the outer part of the incoming boundary layer, the subvolume indicated by the yellow box in figure 11(*a*) is rendered in greater detail in figure 12. The results show semitransparent vorticity magnitude isosurfaces for $|\boldsymbol{\omega}|\delta/U_\infty = 0.5$, half the value for the appropriate visualization of vortical structures closer to the wall, along with velocity vectors in a convective frame of reference of $0.8U_\infty$. Flooded streamwise velocity contours are also shown in the streamwise–spanwise plane. A large-scale rotating bulge can be observed in the centre-left of the figure, as indicated by tangent vectors in the streamwise–wall-normal plane. This swirling pattern is approximately 0.5δ in length and has a convection velocity of around $0.8U_\infty$. The major vorticity component is parallel with the wall and normal to the free-stream direction. Such a feature has been found by Smith & Smits (1995) in the outer layer of their supersonic boundary layer, which they refer to as a 'large-scale bulge'. These authors also discuss how such bulges may support Reynolds shear stress by acting as a pump, drawing high-momentum fluid down into the boundary layer. Indeed, ingested fluid can be seen both upstream and downstream of the structure shown in figure 12, as evidenced by the velocity vectors. This fluid exchange extends from the undisturbed boundary layer edge ($z/\delta = 1.0$) deep into the boundary layer ($z/\delta\ =\ 0.6$), as part of the intermittency process.

The tomographic data also enable streamlines to be traced out throughout the complete three-dimensional measurement domain, to reveal the three-dimensional instantaneous flow topology. These streamlines are computed within the convective reference frame $0.8U_\infty$ and are also shown in figure 12, coloured by instantaneous streamwise velocity. The instantaneous streamline topology depicts a large-scale swirling pattern, in the form of a distorted helicoidal bundle of streamlines, which can

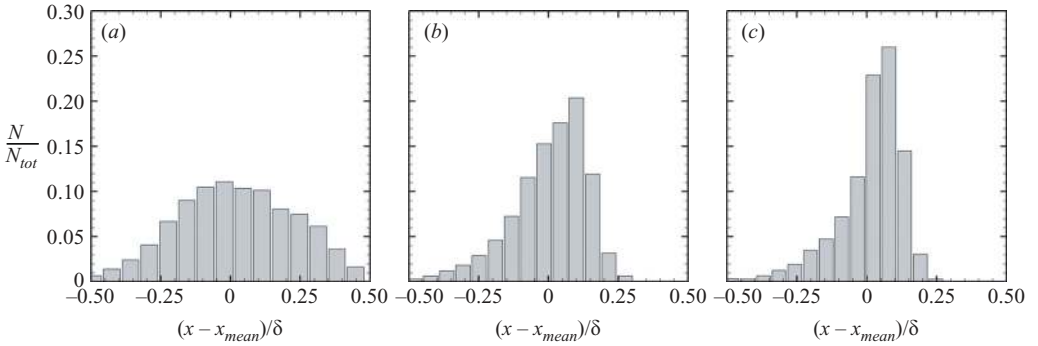

FIGURE 13. Discrete PDFs of the reflected shock wave surrogate position $(x - x_{mean})/\delta$ at various distances from the wall. (*a*) $z/\delta = 0.12$, (*b*) $z/\delta = 0.43$, (*c*) $z/\delta = 0.82$.

be seen to pass through the large-scale rotating bulge, and quickly degenerate outside the vector plane. Although the appearance of such a representation is obviously sensitive to the way in which it is visualized, the results are consistent with an active incoming boundary layer, which exhibits a large-scale organized structure as it enters the interaction.

The effect of these motions on the spatial organization of the reflected shock wave pattern is important. All parts of figure 11 show that the reflected shock wave pattern is more uniform in the spanwise direction, and appears to undergo a relatively smaller streamwise motion than observed closer to the wall. However, streamwise-elongated regions of relatively low-speed fluid can still be occasionally observed at this height, which noticeably affect the reflected shock wave region, as shown in figure 11(*b*) for example. Overall, these results are consistent with the observations made by Dupont *et al.* (2006) in their incident SWTBLI, who recorded hot-wire signals and wall pressure fluctuations simultaneously at the reflected shock wave's mean position, and were able to deduce that the reflected shock wave's length of excursion decreases with distance from the wall.

4.6. *Statistical analysis*

In order to substantiate some of the key observations made above, a statistical analysis is carried out. To characterize the reflected shock wave's behaviour with distance from the wall, the streamwise position of velocity isosurfaces $(x - x_{mean})/\delta$ (where x_{mean} is the mean position) is used as a surrogate for the streamwise position of the reflected shock wave, similar to the approach of Ganapathisubramani *et al.* (2007), who computed the instantaneous separation point using a velocity threshold criterion. Velocity thresholds of $0.75U_\infty$, $0.8U_\infty$, and $0.85U_\infty$ are chosen to characterize the shock wave position at the wall-normal positions $z/\delta = 0.12$, 0.43, and 0.82, respectively. This velocity range has been found to closely correspond to the reflected shock wave region within the boundary layer (see Humble *et al.* 2007). It is important to emphasize that the qualitative trends of the results to be discussed do not change with relatively small variations in the threshold values chosen.

At each spatial location where a velocity vector is obtained, an ensemble of order 200 isosurface positions is determined. From this ensemble, discrete probability density functions (PDFs) are generated, which indicate the relative probability of the isosurface's ith streamwise position $(x/\delta)_i$ falling within a range $(x/\delta)_1 < (x/\delta)_i < (x/\delta)_1 + \Delta(x/\delta)$, where $\Delta(x/\delta)$ is the bin width of the PDF, taken as approximately 0.05 in the present study. A series of PDFs are shown in figure 13,

computed for all spanwise locations at the various distances from the wall. Figure 13(*a*) suggests that relatively close to the wall at $z/\delta = 0.12$, the reflected shock wave region undergoes a relatively large streamwise motion that is of the order of the boundary layer thickness. In contrast, the PDFs in figure 13(*b*, *c*) appear much narrower, consistent with the expectation that the reflected shock wave's streamwise motion decreases with distance from the wall. Note also, that the mean and median positions do not precisely coincide with each other.

To establish a statistical relationship between the flow organization of the incoming boundary layer and reflected shock wave position, streamwise velocity fluctuations within the incoming boundary layer u'/U_∞ are compared with the reflected shock wave surrogate's instantaneous streamwise position, as carried out by Ganapathisubramani *et al.* (2007). The streamwise location $x/\delta = -2.7$ was chosen to obtain the velocity data for each spanwise location, although the results to be discussed were found to be relatively insensitive to small variations in the streamwise location chosen. This is consistent with the long tails found in the autocorrelation function of the streamwise velocity component (see e.g. Ringuette *et al.* 2008; Hutchins & Marusic 2007; Ganapathisubramani *et al.* 2006).

Figure 14 shows the distributions of u'/U_∞ with $(x - x_{mean})/\delta$ on the left, and joint PDFs of u'/U_∞ and $(x - x_{mean})/\delta$ on the right, at the various distances from the wall. Figure 14(*a*, *b*) indicates that relatively close to the wall at $z/\delta = 0.12$, the streamwise velocity fluctuation range within the incoming boundary layer is approximately $-0.1 < u'/U_\infty < 0.1$, corresponding to a net velocity range of $0.2U_\infty$ ($100\,\mathrm{m\,s^{-1}}$), in agreement with the range reported by Ganapathisubramani *et al.* (2007). It is evident that the contours of equiprobability appear elliptical, with the major-axis of the ellipse inclined with respect to the abscissa, again consistent with the observations made by Ganapathisubramani *et al.* (2007). This indicates that when negative streamwise velocity fluctuations are present within the incoming boundary layer ($u' < 0$), then the reflected shock wave is more likely to be located upstream of its median position, and when positive streamwise velocity fluctuations are present within the incoming boundary layer ($u' > 0$), then the reflected shock wave is more likely to be located downstream of its median position. This substantiates the relationship between the low- and high-speed regions within the incoming boundary layer and the reflected shock wave pattern. Such a conclusion is also consistent with the results obtained by Beresh *et al.* (2002) in their compression ramp interaction, who carried out a conditional analysis on planar PIV data in the streamwise–wall-normal plane, and found that positive fluctuations within the incoming boundary layer corresponded to a downstream shock position, and vice versa. The correlation coefficient between u'/U_∞ and $(x - x_{mean})/\delta$ at this distance from the wall is about 0.5, in good agreement with the value of 0.4 reported by Ganapathisubramani *et al.* (2007), as well as the value of about 0.5 reported by Wu & Martin (2008), who carried out the same type of analysis in their DNS study of a compression ramp interaction.

Figure 14(*c*–*f*) shows that the streamwise velocity fluctuation range decreases with distance from the wall to about $-0.1 < u'/U_\infty < 0.05$ by $z/\delta = 0.82$, corresponding to a net velocity range of $0.15U_\infty$ ($75\,\mathrm{m\,s^{-1}}$). The contours of equiprobability now appear much more circular and compact, and this is accompanied by a decrease in the correlation coefficient to below 0.4. Observe, however, how relatively large lobes of probability within the $u' < 0$ and $x < x_{mean}$ region can still be observed at this distance from the wall. This is associated with the occasional passage of relatively low-speed regions throughout the interaction, as can be seen in figure 11(*b*) for instance. In comparison, the distance between adjacent lines of equiprobability rapidly decreases

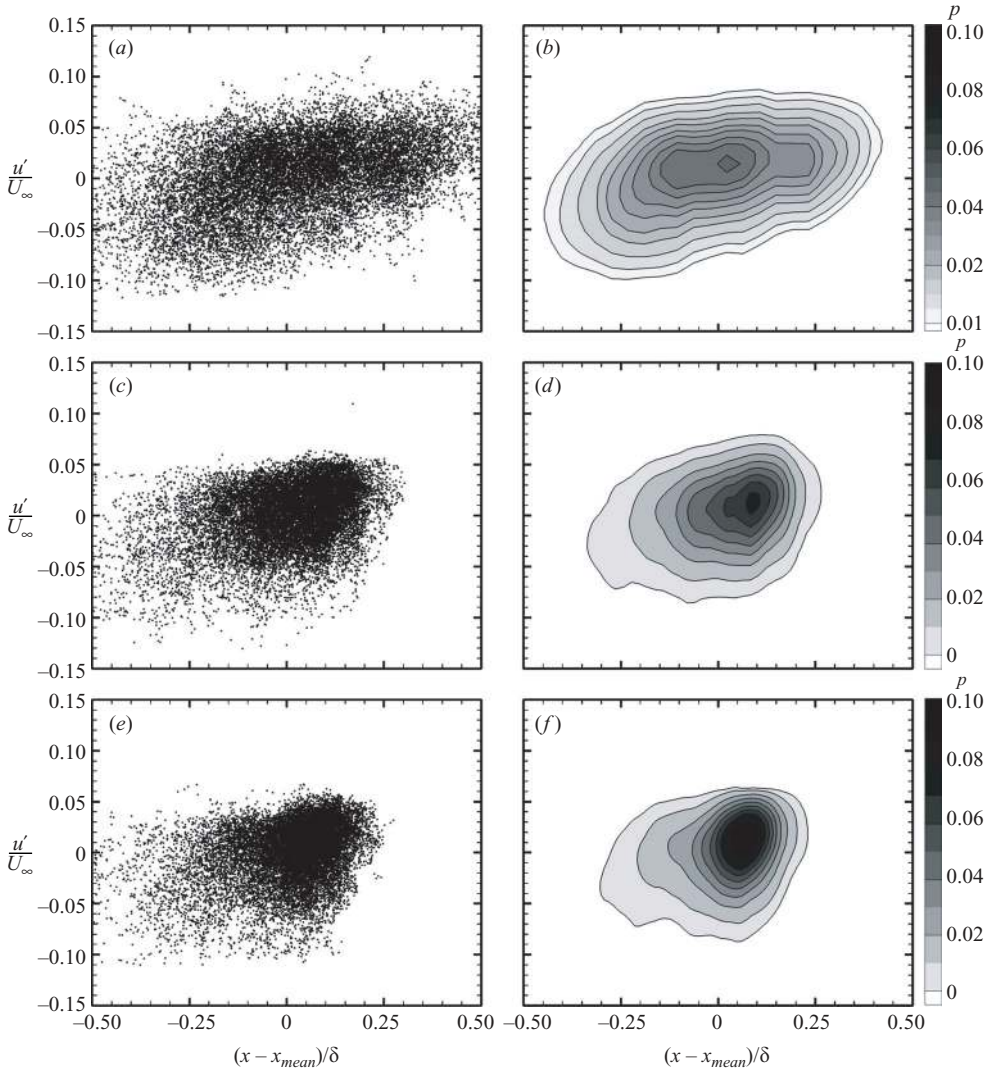

FIGURE 14. Statistical relationship between incoming boundary layer velocity fluctuations u'/U_∞ and streamwise position of the reflected shock wave surrogate $(x - x_{mean})/\delta$ at various distances from the wall. Data are taken at $x/\delta = -2.7$ for each spanwise location. The distributions of u'/U_∞ with $(x - x_{mean})/\delta$ and joint PDFs of u'/U_∞ and $(x - x_{mean})/\delta$ are shown on the left and right, respectively. (a, b) $z/\delta = 0.12$, (c, d) $z/\delta = 0.43$, (e, f) $z/\delta = 0.82$.

for $u' > 0$ and $x > x_{mean}$, indicating that the probability of observing both a relatively high-speed region and a downstream reflected shock wave position decreases with distance from the wall.

5. Summary and discussion

The major observations reported in this study are consolidated to formulate an idealized conceptual model of the interaction's unsteady flow organization. The hairpin vortex packet model can be used to explain the phenomenology observed within the incoming boundary layer, by asserting that the backflow created by several

vortical structures in quasi-streamwise alignment perpetuates the regions of low-speed fluid within the incoming boundary layer, giving rise to the formation of alternating low- and high-speed regions. The high-speed regions typically contain no vortical structures, and exhibit a three-dimensional spanwise sinuous or undulating motion, meandering between the surrounding vortical structures. This behaviour is consistent with a spanwise staggered array of vortical structures, and is a clear indication of the three-dimensionality of the process.

As the interaction is approached, regions containing Q2 ejection events develop within the reflected shock wave region as the outer supersonic fluid within the boundary layer is displaced due to the dilatation of the inner subsonic fluid. This ejection process is highly three-dimensional, with the ejection of fluid varying significantly across the span of the interaction. The reflected shock wave region is also the nucleation site for the onset of vorticity. Interconnecting chains of vorticity are present, thought to be the remnants of spanwise roller-type structures, and are most likely to be associated with the formation of a mixing layer and its subsequent evolution. As the vortical structures propagate through the interaction, they undergo a significant spatial reorganization, being lifted away from the wall, typically losing their identity farther downstream.

The large-scale coherent motions within the incoming boundary layer affect the spatial organization of the reflected shock wave. As the low- and high-speed regions enter the interaction, the reflected shock wave pattern responds to the local incoming conditions that it experiences. High-speed fluid is able to negotiate the adverse pressure gradient better than low-speed fluid, and thus, when a relatively high-speed region enters the interaction, it displaces the reflected shock wave region downstream of its median position. Conversely, when a relatively low-speed region enters the interaction, the reflected shock wave region moves upstream of its median position. The spatial organization of the low- and high-speed regions therefore gives rise to the streamwise translation and spanwise rippling patterns of the reflected shock wave region, and one can see how this behaviour, when viewed in the lower-dimensional representation of a streamwise–wall-normal cross-sectional plane, could give rise to the appearance of the more or less random shock motion behaviour reported in numerous experiments (see e.g. Dolling & Murphy 1983; Ünalmis & Dolling 1998; Dolling 2001; Beresh *et al.* 2002).

Farther from the wall, changes in the incoming boundary layer's flow organization take place, which have important consequences for the reflected shock wave pattern. Flow features within the incoming boundary layer become more spatially disorganized and uncorrelated with the flow phenomenology closer to the wall, as well as the presence of boundary layer intermittency. The overall velocity range decreases, and hence the velocity fluctuations and gradients become weaker. As a result, the shock wave pattern becomes more uniform in the spanwise direction, and undergoes a relatively smaller streamwise motion with distance from the wall. Large-scale organized motions are still occasionally observed, however, in the form of streamwise-elongated regions of relatively low-speed fluid, as well as rotating bulges near the boundary layer edge. The latter in particular, is associated with fluid being ingested from the free stream deep into the boundary layer. A schematic of the three-dimensional model showing the main phenomenological features is shown in figure 15.

While the present study has put forth evidence for a relationship between the phenomenology within the incoming boundary layer and instantaneous flow organization of the interaction, there have been somewhat alternative yet possibly

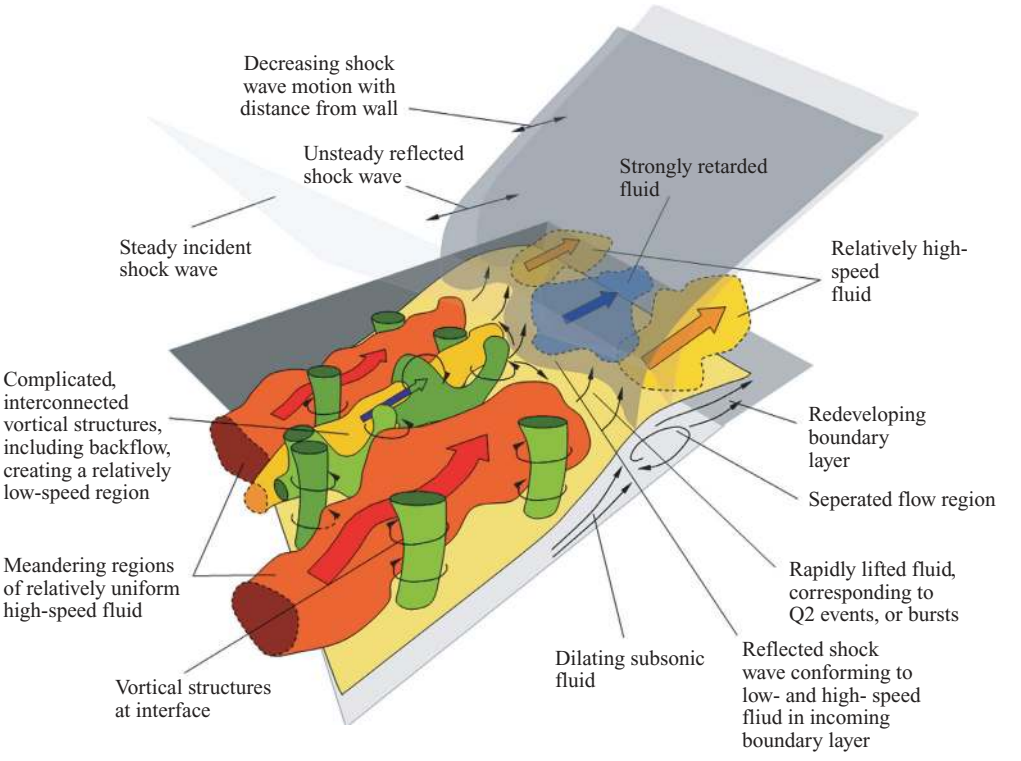

FIGURE 15. Schematic representation of the three-dimensional physical model. Shown are the three-dimensional low- and high-speed regions within the incoming boundary layer. Vortical structures are associated with the relatively low-speed regions, whereas relatively high-speed regions fill-in the separation between these structures. Fluid entering the interaction is rapidly lifted away from the wall, as part of a highly three-dimensional Q2 ejection event process. The corresponding streamwise translation and spanwise rippling patterns of the reflected shock wave are also indicated, whose streamwise motion decreases with distance from the wall.

related explanations for the large-scale unsteadiness observed in SWTBLIs. As far as the shock reflection case is concerned, recall that Pirozzoli & Grasso (2006) have emphasized the internal dynamics of the separated flow region, proposing an acoustic feedback mechanism. In addition, Dupont *et al.* (2006) have shown that the reflected shock wave motion and downstream part of the interaction appear to be strongly linked at low frequency. Such behaviour has also been found by Thomas *et al.* (1994) in their compression ramp interaction. It is therefore not inconceivable to suppose that several mechanisms associated with the large-scale unsteadiness coexist. The number of divergent theories present in the literature that attempt to explain the cause(s) of the large-scale unsteadiness seems to suggest that this is the case. The current research has provided a model based on one such mechanism associated with the incoming boundary layer, which seems to be pertinent to the unsteady behaviour of the present interaction.

6. Conclusions

An experimental study has been carried out to investigate the three-dimensional instantaneous structure of an incident SWTBLI at Mach 2.1 using tomographic PIV. As a result, several conclusions can be drawn.

Tomographic PIV is well-suited to the investigation of the three-dimensional instantaneous structure of SWTBLIs, and reduces the complexity and ambiguity of cross-sectional representations by providing a volumetric synthesis of the results.

The incoming boundary contains large-scale coherent motions, in the form of three-dimensional streamwise-elongated regions of relatively low- and high-speed fluid, similar to what has been observed in other subsonic and supersonic boundary layers. Distinct regions of vorticity are present within the incoming boundary layer, forming spatially compact regions that exhibit a range of shape and size. They appear in a quasi-streamwise alignment, and are located within the relatively low-speed regions and at the interface between the low- and high-speed regions, in a way that can be explained by the hairpin packet model of incompressible boundary layers. The phenomenology found in incompressible boundary layers therefore portrays an underlying similarity in the supersonic flow regime.

The reflected shock wave pattern is affected by the flow organization of the incoming boundary layer. Observations of the instantaneous velocity fields, supported by a statistical analysis, suggest that the reflected shock wave region conforms to the streamwise-elongated low- and high-speed regions within the incoming boundary layer as they enter the interaction. Its organization can be qualitatively decomposed into overall streamwise translation and spanwise rippling patterns, in agreement with the observations made in compression ramp interactions. Farther from the wall, the streamwise motion of the reflected shock wave region decreases and appears more uniform in the spanwise direction. It therefore seems that the large-scale unsteadiness of incident shock wave and compression ramp interactions share some important physical features.

This work is supported by the Dutch Technology Foundation STW under the VIDI – *Innovation Impulse* program, grant DLR.6198. LaVision GmbH is gratefully acknowledged for the provision of the tomographic PIV system. The authors also thank the reviewers for their helpful suggestions in the preparation of this paper.

REFERENCES

Adamson, T. C. Jr & Messiter, A. F. 1980 Analysis of two-dimensional interactions between shock waves and boundary layers. *Annu. Rev. Fluid Mech.* **12**, 103–138.

Adrian, R. J., Meinhart, C. D. & Tomkins, C. D. 2000 Vortex organization in the outer region of the turbulent boundary layer. *J. Fluid Mech.* **442**, 1–54.

Andreopoulos, J. & Muck, K. C. 1987 Some new aspects of the shock-wave/boundary-layer interaction in compression-ramp flows. *J. Fluid Mech.* **180**, 405–428.

Beresh, S. J., Clemens, N. T. & Dolling, D. S. 2002 Relationship between upstream turbulent boundary-layer velocity fluctuations and separation shock unsteadiness. *AIAA J.* **40**, 2412–2422.

Bookey, P., Wyckham, C. & Smits, A. J. 2005 Experimental investigations of Mach 3 shock-wave turbulent boundary layer interactions. *AIAA Paper* 2005-4899.

Brucker, C. 1996 3-D Scanning particle image velocimetry: technique and application to a spherical cap wake flow. *Appl. Sci. Res.* **56**, 157–179.

Chong, M. S., Soria, J., Perry, A. E., Chacin, J., Cantwell, B. J. & Na, Y. 1998 Turbulence structures of wall-bounded shear flows using DNS data. *J. Fluid Mech.* **357**, 225–247.

Délery, J. & Marvin J. G. 1986 Shock-wave boundary layer interactions. *AGARDograph* 280.

Delo, C. J., Kelso, R. M. & Smits, A. J. 2004 Three-dimensional structure of a low-Reynolds-number turbulent boundary layer. *J. Fluid Mech.* **512**, 47–83.

Dolling, D. S. 2001 Fifty years of shock wave/boundary layer interaction research: what next? *AIAA J.* **39**, 1517–1531.

Dolling, D. S. & Murphy, M. T. 1983 Unsteadiness of the separation shock wave structure in a supersonic compression ramp flowfield. *AIAA J.* **21**, 1628–1634.

Dupont, P., Haddad, C. & Debiève, J. F. 2006 Space and time organization in a shock-induced separated boundary layer. *J. Fluid Mech.* **559**, 255–277.

Dussauge, J.-P., Dupont, P. & Debiève, J. F. 2006 Unsteadiness in shock wave boundary layer interactions with separation. *Aero. Sci. Technol.* **10**, 85–91.

Elena, M. & Lacharme, J. P. 1988 Experimental study of a supersonic turbulent boundary layer using a laser Doppler anemometer. *J. Theor. Appl. Mech.* **7**, 175–190.

Elsinga, G. E. 2008 Tomographic particle image velocimetry: and its application to turbulent boundary layers. PhD Thesis, Faculty of Aerospace Engineering, Delft University of Technology, Delft, The Netherlands.

Elsinga, G. E., Adrian, R. J., van Oudheusden, B. W. & Scarano, F. 2007*a* Tomographic-PIV investigation of a high Reynolds number turbulent boundary layer. In *Proc. 7th Intl Symp. on Particle Image Velocimetry*, *Rome*, *Italy*, *Sep. 11–14.*

Elsinga, G. E., Kuik, D. J., van Oudheusden, B. W. & Scarano, F. 2007*b* Investigation of the three-dimensional coherent structures in a turbulent boundary layer with tomographic-PIV. In *Proc. 45th AIAA Aerospace Sciences Meeting & Exhibit*, *Reno. NV. Jan. 8–11.*

Elsinga, G. E., Scarano, F., Wieneke, B. & van Oudheusden, B. W. 2006 Tomographic particle image velocimetry. *Exps. Fluids* **41**, 933–947.

Elsinga, G. E., van Oudheusden, B. W. & Scarano, F. 2005 Evaluation of aero-optical distortion effects in PIV. *Exps. Fluids* **39**, 246–256.

Erengil, M. E. & Dolling, D. S. 1993 Physical causes of separation shock unsteadiness in shock wave/turbulent boundary layer interactions. *AIAA Paper* 93-3134.

Ganapathisubramani, B., Clemens, N. T. & Dolling, D. S. 2006 Large-scale motions in a supersonic turbulent boundary layer. *J. Fluid Mech.* **556**, 271–282.

Ganapathisubramani, B., Clemens, N. T. & Dolling, D. S. 2007 Effects of upstream boundary layer on the unsteadiness of shock-induced separation. *J. Fluid Mech.* **585**, 369–394.

Ganapathisubramani, B., Hutchins, N., Hambleton, W. T., Longmire, E. K. & Marusic, I. 2005 Investigation in a turbulent boundary layer using two-point correlations. *J. Fluid Mech.* **524**, 57–80.

Ganapathisubramani, B., Longmire, E. K. & Marusic, I. 2003 Characteristics of vortex packets in turbulent boundary layers. *J. Fluid Mech.* **478**, 35–46.

Green, J. E. 1970 Interactions between shock waves and turbulent boundary layers. *Prog. Aero. Sci.* **11**, 253–340.

Hankey, W. L. Jr. & Holden, M. S. 1975 Two-dimensional shock-wave boundary layer interactions in high-speed flows. *AGARDograph* 203.

Head, M. R. & Bandyopadhyay, P. 1981 New aspects of turbulent boundary-layer structure. *J. Fluid Mech.* **107**, 297–338.

Herman, G. T. & Lent, A. 1976 Iterative reconstruction algorithms. *Comput. Biol. Med.* **6**, 273–294.

Hinsch, K. D. 2002 Holographic particle image velocimetry. *Meas. Sci. Technol.* **13**, R61–R72.

Hou, Y. X. 2003 Particle image velocimetry study of shock-induced turbulent boundary layer separation. PhD Thesis, Department of Aerospace Engineering and Engineering Mechanics, The University of Texas at Austin.

Humble, R. A., Scarano, F. & van Oudheusden, B. W. 2007 Particle image velocimetry measurements of a shock wave/turbulent boundary layer interaction. *Exps. Fluids* **43**, 173–183.

Hutchins, N. & Marusic, I. 2007 Evidence of very long meandering features in the logarithmic region of turbulent boundary layers. *J. Fluid Mech.* **579**, 1–28.

Kim, K. C. & Adrian, R. J. 1999 Very large-scale motion in the outer layer. *Phys. Fluids* **11**, 417–422.

Klebanoff, P. 1955 Characteristics of turbulence in a boundary layer with zero pressure gradient. *NACA Rep.* 1247.

Knight, D. D. & Degrez, G. 1998 Shock wave boundary layer interactions in high speed flows: a critical survey of current numerical prediction capabilities. *Advisory Rep.* 319, AGARD 2:1. 1–1.35.

Na, Y. & Moin, P. 1998 Direct numerical simulation of a separated turbulent boundary layer. *J. Fluid Mech.* **374**, 379–405.

Pereira, F. & Gharib, M. 2002 Defocusing digital particle image velocimetry and the three-dimensional characterization of two-phase flows. *Meas. Sci. Technol.* **13**, 683–694.

Pirozzoli, S. & Grasso, F. 2006 Direct numerical simulation of impinging shock wave/turbulent boundary layer interaction at $M = 2.25$. *Phys. Fluids* **18**, 065113.

Plotkin, K. J. 1975 Shock wave oscillation driven by turbulent boundary-layer fluctuations. *AIAA J.* **13**, 1036–1040.

Poggie, J. & Smits, A. J. 2001 Shock unsteadiness in a reattaching shear layer. *J. Fluid Mech.* **429**, 155–185.

Ringuette, M. J., Wu, M. & Martin, M. P. 2008 Coherent structures in direct numerical simulation of turbulent boundary layers at Mach 3. *J. Fluid Mech.* **594**, 59–69.

Samimy, M., Arnette, S. A. & Elliot, G. S. 1994 Streamwise structures in a turbulent supersonic boundary layer. *Phys. Fluids* **6**, 1081–1083.

Samimy, M. & Lele, S. K. 1991 Motion of particles with inertia in a compressible free shear layer. *Phys. Fluids* **3**, 1915–1923.

Schrijer, F. F. J. & Scarano, F. 2007 Particle slip compensation in steady compressible flows. In *Proc. 7th Intl Symposium on Particle Image Velocimetry, Rome, Italy, Sept. 11–14.*

Schrijer, F. F. J., Scarano, F. & van Oudheusden, B. W. 2006 Application of PIV in a Mach 7 double-ramp flow. *Exps. Fluids* **41**, 353–363.

Schröder, A., Geisler, R., Elsinga, G. E., Scarano, F. & Dierksheide, U. 2007 Investigation of a turbulent spot and a tripped turbulent boundary layer flow using time-resolved tomographic PIV. *Exps. Fluids* **44**, 305–316.

Smith, M. W. & Smits, A. J. 1995 Visualization of the structure of supersonic turbulent boundary layers. *Exps. Fluids* **18**, 288–302.

Smits, A. J. & Dussauge, J.-P. 2006 *Turbulent Shear Layers in Supersonic Flow*, 2nd Edn. American Institute of Physics.

Soloff, S. M., Adrian, R. J. & Liu, Z.-C. 1997 Distortion compensation for generalized stereoscopic particle image velocimetry. *Meas. Sci. Technol.* **8**, pp. 1441–1454.

Spina, E. F., Donovan, J. F. & Smits, A. J. 1991 On the structure of high-Reynolds-number supersonic turbulent boundary layers. *J. Fluid Mech.* **222**, 293–327.

Thomas, F. O., Putman, C. M. & Chu, H. C. 1994 On the mechanism of unsteady shock oscillation in shock wave/turbulent boundary layer interaction. *Exps. Fluids* **18**, 69–81.

Tomkins, C. D. & Adrian, R. J. 2003 Spanwise structure and scale growth in turbulent boundary layers. *J. Fluid Mech.* **490**, 37–74.

Ünalmis, Ö. H. & Dolling, D. S. 1998 Experimental study of causes of unsteadiness of shock-induced turbulent separation. *AIAA J.* **36**, 371–378.

Westerweel, J. & Scarano, F. 2005 Universal outlier detection for PIV data. *Exps. Fluids* **39**, 1096–1100.

Wieneke, B. 2007 Volume self-calibration for stereo-PIV and tomographic-PIV. In *Proc. 7th Intl Symp. on Particle Image Velocimetry, Rome, Italy, Sep. 11–14.*

Wu, M. & Martin, M. P. 2007 Direct numerical simulation of supersonic turbulent boundary layer over a compression ramp. *AIAA J.* **45**, 879–889.

Wu, M. & Martin, M. P. 2008 Analysis of shock motion in shockwave and turbulent boundary layer interaction using direct numerical simulation data. *J. Fluid Mech.* **594**, 71–83.